On the Origins of Vorticity in a Simulated Tornado-Like Vortex

JOHANNES M. L. DAHL[a] AND JANNICK FISCHER[a]

[a] *Department of Geosciences, Texas Tech University, Lubbock, Texas*

(Manuscript received 27 June 2022, in final form 19 January 2023)

ABSTRACT: The authors explore the dynamical origins of rotation of a mature tornado-like vortex (TLV) using an idealized numerical simulation of a supercell thunderstorm. Using 30-min forward parcel trajectories that terminate at the base of the TLV, the vorticity dynamics are analyzed for $n = 7$ parcels. Aside from the integration of the individual terms of the traditional vorticity equation, an alternative formulation of the vorticity equation and its integral, here referred to as vorticity source decomposition, is employed. This formulation is derived on the basis of Truesdell's "basic vorticity formula," which is obtained by first formulating the vorticity in material (Lagrangian) coordinates, and then obtaining the components relative to the fixed spatial (Eulerian) basis by applying the vector transformation rule. The analysis highlights surface drag as the most reliable vorticity source for the rotation at the base of the vortex for the analyzed parcels. Moreover, the vorticity source decomposition exposes the importance of small amounts of vorticity produced baroclinically, which may become significant after sufficient stretching occurs. Further, it is shown that ambient vorticity, upon being rearranged as the trajectories pass through the storm, may for some parcels directly contribute to the rotation of the TLV. Finally, the role of diffusion is addressed using analytical solutions of the steady Burgers–Rott vortex, suggesting that diffusion cannot aid in maintaining the vortex core.

KEYWORDS: Trajectories; Supercells; Tornadoes; Vorticity; Cloud resolving models; Coordinate systems

1. Introduction

Recent work on the vorticity dynamics of supercell tornadoes has emphasized the transition of the dominant processes by which parcels acquire near-surface vertical vorticity during tornadogenesis. First, regions of surface vertical vorticity (vortex patches) appear within outflow air of the supercell. The production of these vortex patches relies on negatively buoyant downdrafts (e.g., Davies-Jones and Brooks 1993; Walko 1993; Dahl et al. 2014; Parker and Dahl 2015). These seed vortex patches tend to axisymmetrize while also amplifying (Dahl 2020), whereupon horizontal vorticity can be tilted upward abruptly within the corner flow of the vortex (Fischer and Dahl 2022, and the references therein).

Since parcels in a supercell's environment carry abundant horizontal vorticity, a question that arises is whether this vorticity can directly feed the tornado (even if a detour through a downdraft may occur). Although the association of tornadoes with strong low-level wind shear has been known for some time (e.g., Rasmussen and Blanchard 1998), so far only indirect effects have been identified by which the ambient vorticity is beneficial to tornadoes. For instance, Markowski and Richardson (2014) and Coffer and Parker (2017) have shown that the more intense and streamwise the ambient vorticity is, the more intense and better organized is the mesocyclone, and the lower its base, implying stronger upward pressure-gradient accelerations. These help lift the vertical-vorticity-bearing outflow air and thus support tornadogenesis and tornado maintenance.

One challenge in analyzing the direct role of ambient vorticity in maintaining tornadoes is that the integral of the traditional vorticity equation (i.e., integrating each term of the vorticity equation separately) merely reveals that, e.g., tilting and stretching dominates, but the origin of the vorticity that is being tilted and stretched cannot be identified. Davies-Jones (2000) pioneered application of a different formulation of the integral of the vorticity equation, often referred to as vorticity decomposition, to idealized supercell-like flows.[1] This vorticity source decomposition allows one to determine the effect of tilting and stretching of the part of the vorticity that has (i) existed initially and (ii) that has subsequently been produced via baroclinic or mixing effects. Dahl et al. (2014) and Dahl (2015) applied a simplified version of this decomposition to the development of vortex patches that serve as seeds for tornadogenesis within the storm's outflow. They found that baroclinically produced and subsequently reoriented vorticity ("baroclinic vorticity") dominates in these vortex patches, and that the average effect of vorticity imported from the environment at best is neutral (Dahl et al. 2014), or in some cases contributes negatively (Dahl 2015). Markowski (2016) applied the vorticity source decomposition to idealized "pseudo-supercell" simulations and found that as the storm matured the main vorticity source of the tornado-like vortices (TLVs) that developed in the simulation was baroclinic vorticity, though the imported ("barotropic") vorticity also contributed. Due to limitations of the numerical integration of the vorticity parts, the analysis by Markowski (2016) focused on vortices relatively early in the simulation, rather than what may be considered mature TLVs. In

Fischer's current affiliation: Karlsruher Institut für Technologie, Karlsruhe, Germany.

Corresponding author: Johannes Dahl, johannes.dahl@ttu.edu

[1] Here we refer to this technique as vorticity *source* decomposition, because the traditional integral of the vorticity equation, discussed in section 3 also constitutes a "decomposition" of the vorticity vector.

DOI: 10.1175/JAS-D-22-0145.1

this paper, the problem is thus revisited by considering a mature, simulated tornado-like vortex in a full-physics simulation, and by using the complete vorticity source decomposition (including numerical and subgrid-scale mixing terms) along 30-min forward-integrated trajectories. We will also contrast the vorticity source decomposition with the traditional integral of the vorticity equation.

In the next section, the simulation will be introduced. In section 3 the vorticity equations, their integrals, and their utility will be reviewed. Further, a derivation of Truesdell's basic vorticity formula utilizing tools from differential geometry will be offered. In section 4 trajectories will be analyzed, and the results will be discussed in section 5. Finally, conclusions are offered in section 6.

2. Model setting

We used the Bryan Cloud Model 1 (CM1; Bryan and Fritsch 2002), release 19, to which parcel diagnostics have been added, such that the velocity gradient, the curl of the pressure-gradient force and of numerical and subgrid-scale (SGS) mixing, as well as the curl of the Coriolis force, are available along the parcel trajectories. These contributions were taken directly from the diagnostics available within CM1, and calculated on the respective staggered grids. The simulation analyzed here is the same as the full-physics simulation of the mature and intense tornado-like vortex analyzed by Fischer and Dahl (2022). The horizontal domain has a size of 200×200 km^2, with a constant horizontal grid spacing of 200 m in the inner portion of the domain ($50 < x < 150$ km), stretched to circa 1.8 km toward the domain boundary. The vertical grid spacing increases from 20 m near the ground to 280 m at the domain top, which is located at about 18 km AGL. Cloud and precipitation processes are parameterized using the double-moment NSSL scheme. The VORTEX2 tornadic composite sounding obtained by Parker (2014) served as base state, and the storm was initiated using the updraft nudging technique as discussed by Fischer and Dahl (2022). The lower boundary condition is semislip, and the lateral boundary conditions are open-radiative. A fifth-order horizontal and vertical advection scheme is employed.

When a semislip boundary condition is used at the lower boundary, a pseudo pressure gradient force needs to be present in order to maintain a quasi-steady environment (without this, the surface flow will continuously lose momentum). One common approach, which is also adopted herein, is to include the Coriolis force, but only allow it to act on the perturbation winds. In the present case this led to minor adjustment of the flow field early in the simulation. Davies-Jones (2021) has warned of some pitfalls in this technique. In this approach, it is implicitly assumed that the base state is in thermal wind balance. Consequently, continued circulation production is implied in a vertical plane due to the baroclinity associated with the thermal wind shear, but this circulation production is balanced by the tilting of planetary vorticity into the horizontal (Davies-Jones 1991). The Coriolis force thus has an effect only on the unbalanced (i.e., ageostrophic) part of the flow. However, since the real wind profile most likely is not geostrophically balanced (due, e.g., to isallobaric effects and surface drag), the effect of the Coriolis force may be erroneous. However, in the traditional integral of the vorticity equation, this effect is negligible (the Coriolis forcing is practically zero for all parcels we investigated). For the vorticity source decomposition (section 3b), the Coriolis effect is nonnegligible but it does not contribute meaningfully to the vorticity budgets as shown in section 4, so this error is unlikely to affect the main results significantly.

A total of 5.4 million trajectories were launched at 2400 s simulation time covering the domain $[100, 145] \times [90, 120] \times [0.01, 1.8]$ km^3. These initial locations were found iteratively as described by Fischer and Dahl (2022). The trajectories were then integrated forward for 30 min. Such long histories are needed if the intention is to decompose the vorticity into parts that stem from (approximately) the environment as well as storm-generated contributions. That is, the parcels ought to begin their journey in the unperturbed environment upstream of the storm. Only parcels that became part of the TLV, i.e., attained vertical vorticity in excess of 0.1 s^{-1} between 20 and 70 m AGL and between 4135 and 4145 s were considered, giving 95 parcels. Of those parcels, the majority dropped below the lowest scalar model level (10 m AGL), rendering them unsuitable for analysis (Vande Guchte and Dahl 2018). This is a rather consequential criterion, because tornadoes are characterized by strong upward motion very close to the ground. This means that there is upward motion at the lowest model level, implying that parcels generally enter the vortex base from below the lowest model level. Looking higher above the ground to identify parcels within the vortex reduces this problem, but these parcels may no longer capture the "near-surface" dynamics. Parcels that enter the vortex in the lowest ~50 m AGL and at the same time have not dipped below the lowest scalar model level are thus very rare.

Moreover, the initial horizontal vorticity of the parcels, rounded to one hundredth, was not allowed to differ from the base-state horizontal vorticity rounded to one hundredth. This was done to ensure that the parcels approximately had the same vorticity as the base state when starting the integration. For most parcels, this meant $\boldsymbol{\omega}_h^{\text{parcel}}(t_0) \approx \boldsymbol{\omega}_h^{\text{environment}} \approx 0.01$ s^{-1}. The initial vertical vorticity was generally on the order of 10^{-4} s^{-1}. Finally, the integrated vorticity had to match sufficiently closely the known total vorticity along the trajectories (this determination was made subjectively). Application of these criteria eliminated the majority of the trajectories from the analysis; however, $n = 7$ parcel trajectories were found to fulfill all requirements, and these parcels will be analyzed in the remainder of the paper.

3. Vorticity equations and their integrals

a. Traditional integration of the vorticity equation

When integrating the vorticity equation (e.g., Markowski and Richardson 2010) each term is integrated separately, which decomposes the vorticity into parts that arise from the tilting and stretching terms, as well as those parts resulting

from the source (or torque) terms. The vorticity equation for the present setting is given by

$$\frac{d\boldsymbol{\omega}}{dt} = \boldsymbol{\omega}\cdot\boldsymbol{\nabla}\mathbf{v} - \boldsymbol{\omega}(\boldsymbol{\nabla}\cdot\mathbf{v}) + \frac{1}{\rho^2}\boldsymbol{\nabla}\rho\times\boldsymbol{\nabla}p + \boldsymbol{\nabla}\times\mathbf{f}_{\text{sgs}} + \boldsymbol{\nabla}\times\mathbf{f}_{\text{diff}} - \boldsymbol{\nabla}\times(f\mathbf{k}\times\mathbf{v}'), \tag{1}$$

where $\boldsymbol{\omega} = \boldsymbol{\nabla}\times\mathbf{v} = (\xi, \eta, \zeta)$ is the vorticity vector, $\mathbf{v}$ is the wind vector, $\mathbf{v}'$ is the perturbation (ageostrophic) wind, p is pressure, ρ is air density, $\mathbf{f}_{\text{sgs}}$ is the acceleration due to SGS mixing, and $\mathbf{f}_{\text{diff}}$ is the acceleration due to numerical diffusion; $f = 10^{-4}\ \text{s}^{-1}$ represents the Coriolis parameter. All variables are evaluated along parcel trajectories and thus only depend on time (and the parcel label, which is omitted here for notational ease). The vorticity, then, is the sum of the integral of each term,

$$\boldsymbol{\omega}_{\text{str/tilt}}(t) = \int_{t_0}^{t} dt'[\boldsymbol{\omega}(t')\cdot\boldsymbol{\nabla}\mathbf{v}(t') - \boldsymbol{\omega}(t')\boldsymbol{\nabla}\cdot\mathbf{v}(t')], \tag{2}$$

$$\boldsymbol{\omega}_{\text{bc}}(t) = \int_{t_0}^{t} dt'\frac{1}{\rho(t')^2}\boldsymbol{\nabla}\rho(t')\times\boldsymbol{\nabla}p(t'), \tag{3}$$

$$\boldsymbol{\omega}_{\text{sgs}}(t) = \int_{t_0}^{t} dt'\boldsymbol{\nabla}\times\mathbf{f}_{\text{sgs}}(t'), \tag{4}$$

$$\boldsymbol{\omega}_{\text{diff}}(t) = \int_{t_0}^{t} dt'\boldsymbol{\nabla}\times\mathbf{f}_{\text{diff}}(t'), \tag{5}$$

$$\boldsymbol{\omega}_{\text{cor}}(t) = -\int_{t_0}^{t} dt'\boldsymbol{\nabla}\times[f\mathbf{k}\times\mathbf{v}'(t')], \tag{6}$$

such that

$$\boldsymbol{\omega}(t) = \boldsymbol{\omega}(t_0) + \boldsymbol{\omega}_{\text{str/tilt}}(t) + \boldsymbol{\omega}_{\text{bc}}(t) + \boldsymbol{\omega}_{\text{sgs}}(t) + \boldsymbol{\omega}_{\text{diff}}(t) + \boldsymbol{\omega}_{\text{cor}}(t). \tag{7}$$

This vorticity decomposition will be referred to as "traditional integral." This formulation yields the separate net contributions due to stretching and tilting ("str" and "tilt") of the total vorticity,[2] baroclinic vorticity production ("bc"), vorticity generation via SGS mixing ("sgs"), as well as via numerical diffusion ("diff"). Stretching and tilting of planetary vorticity is described by $\boldsymbol{\omega}_{\text{cor}}$. A practical advantage of this formulation is that it can be integrated using a simple trapezoidal scheme (see appendix B) because $\boldsymbol{\nabla}\mathbf{v}$ (including $\boldsymbol{\omega}$) as well as the source terms, are available along the entire trajectory.

b. *Vorticity source decomposition: Truesdell's basic vorticity formula*

An alternative way of decomposing the vorticity vector is based on Truesdell's "basic vorticity formula" (Truesdell 1954, p. 154). An elegant way of obtaining it is afforded by the use of the material (Lagrangian) coordinate system. This system is made up of a coordinate grid that moves with the flow and is deformed along the way (e.g., Salmon 1998, p. 5). The derivation here utilizes classical tensor calculus following, e.g., Truesdell (1954) and Dutton (1976), and it extends the treatment by Dahl et al. (2014, their appendix A) by leveraging the material description of vorticity. The reader is referred to the extensive work by Davies-Jones (2000, 2006, 2015, 2022) for alternative derivations and formulations applicable to specific flows and configurations with an eye to supercell-like flows, and Epifanio and Durran (2002) for applications to orographic vortices.

The basic premise of our derivation is that physical laws or quantities should not depend on the observer. Thus, one may choose any coordinate system while the laws of physics ought to be unchanged (e.g., Zee 2013, p. 68). However, when changing the coordinate basis vectors associated with one coordinate system (ξ^α) to another (x^i), a given vector $\mathbf{a}$ has its components changed according to the law

$$a^i = \frac{\partial x^i}{\partial \xi^\alpha}\hat{a}^\alpha, \tag{8}$$

which ensures that the vector itself remains unchanged. Here, a^i represent the components with respect to the x^i coordinate basis, and $\hat{a}^\alpha$ are the components with respect to the ξ^α coordinate basis. In 3D, one may think of the vector as a rigid arrow, and the above transformation law ensures that the arrow's projections on the new coordinate basis leave the arrow itself unchanged. Physical quantities that exhibit this transformation behavior under general coordinate transformations are characterized by "general covariance" (e.g., Zee 2013, p. 47). This principle will be utilized by formulating the vorticity vector first in material coordinates and then obtaining the desired components relative to the spatial basis simply by applying the coordinate transformation matrix.

To begin, we introduce the fixed spatial (Eulerian) coordinates x^i and the time-dependent material (Lagrangian) coordinates ξ^α. In addition, in classical tensor analysis there always exist background Cartesian coordinates y^j, relative to which the other coordinate systems and their coordinate basis vectors are defined (e.g., Marsden and Hughes 1983, p. 44).

All indices run from 1 to 3, where the spatial components have Roman letters as indices, and the material components are represented by Greek letters. That is, the components a^i of a vector $\mathbf{a}$ pertain to the spatial basis, and the components a^α pertain to the material basis. The fixed spatial coordinates are assumed to be non-Cartesian to keep the analysis as general as possible, though practically the spatial coordinates are often taken to be Cartesian. The material coordinates, in the present interpretation, remain attached to each fluid parcel and are given by the spatial coordinates that the parcels occupy at some arbitrary reference time t_0. Throughout, Einstein's summation convention is used. The reader is referred to Simmonds (1994) for some background on classical tensor calculus in curvilinear coordinates. The advantage of using material coordinates is that the vorticity equation and its integral are comparatively simple in these coordinates. Davies-Jones (2022) leveraged this observation by writing the evolution equation of vorticity in material coordinates, which allowed for a straightforward integration. The

[2] If the individual components are written out, the traditional "tilting" and "stretching" terms can be isolated; e.g., $d\zeta/dt|_{\text{str/tilt}} = -\zeta(\boldsymbol{\nabla}\cdot\mathbf{v}) + \boldsymbol{\omega}_h\cdot\boldsymbol{\nabla}_h w + \zeta\partial w/\partial z = -\zeta(\boldsymbol{\nabla}_h\cdot\mathbf{v}_h) + \boldsymbol{\omega}_h\cdot\boldsymbol{\nabla}_h w$, which are the conventional stretching and tilting terms.

starting point of our approach is the expression for vorticity itself and subsequent use of a simple integral of the momentum equation to obtain the desired vorticity formulas.

Here we are interested in the contravariant components of the vorticity vector, because these pertain to the local covariant basis vectors, which are parallel to the coordinate axes, and lengthen/shorten in the same way as the coordinate axes upon deformation. The contravariant vorticity components thus naturally embody the effects of deformation on vortex line segments (e.g., Dahl et al. 2014; Davies-Jones 2022). The curl of the velocity field $\mathbf{u}$ in arbitrary curvilinear coordinates x^i is given by

$$(\boldsymbol{\nabla}\times\mathbf{v})^k=\omega^k=\frac{\epsilon^{ijk}}{\sqrt{g}}\frac{\partial u_j}{\partial x^i}, \tag{9}$$

where u_j represents the covariant velocity components, ω^k represents the vorticity vector, ϵ^{ijk} is the permutation symbol, and g is the determinant of the metric tensor $\mathbf{g}$, pertaining to the x^i coordinates. It can be shown that $\sqrt{g}=J_x^y$, where J_x^y is the Jacobian, i.e., the determinant of the transformation matrix from the curvilinear x^i coordinates to the Cartesian frame y^i.[3] The Jacobian equals the ratio of volume elements in each coordinate system (e.g., Aris 1962, p. 83), so for instance,

$$J_\xi^x=\frac{V(t)}{V(t_0)}=\frac{\rho(t_0)}{\rho(t)}, \tag{10}$$

where in the last-step mass conservation was assumed. If the Jacobian (or the determinant of the metric tensor) is omitted from the definition of the curl [Eq. (9)], only volume-preserving transformations without reflections are permitted (e.g., proper rotations), or else the components of the curl do not transform correctly.

We start by writing the vorticity vector in the time-dependent material frame:

$$[\boldsymbol{\nabla}\times\mathbf{v}(t)]^\gamma=\omega^\gamma(t)=\frac{\epsilon^{\alpha\beta\gamma}}{\sqrt{G(t)}}\frac{\partial u_\beta(t)}{\partial\xi^\alpha}. \tag{11}$$

Here $G(t)$ is time dependent in the general case of compressible flows, because a given material volume element will expand or compress compared to its initial volume. To obtain the vorticity formula, one merely has to rewrite u_β as an integral of the material acceleration. Starting with Newton's second law,

$$\frac{\delta u_\beta(t)}{\delta t}=f_\beta(t), \tag{12}$$

where f_β represents the covariant components of the net force $\mathbf{f}$ acting on the parcel and the $\delta/\delta t$ operator is the material derivative (see appendix A). Then the material velocity is given by

$$u_\beta(t)=u_\beta(t_0)+\int_{t_0}^{t}dt' f_\beta(t'). \tag{13}$$

The vorticity in the material picture is then simply obtained by inserting Eq. (13) into Eq. (11):

$$\omega^\gamma=\frac{\epsilon^{\alpha\beta\gamma}}{\sqrt{G(t)}}\frac{\partial u_\beta(t_0)}{\partial\xi^\alpha}+\int_{t_0}^{t}dt'\frac{\epsilon^{\alpha\beta\gamma}}{\sqrt{G(t)}}\frac{\partial f_\beta(t')}{\partial\xi^\alpha}. \tag{14}$$

This equation may be written in a more insightful manner. Starting with the first term, and remembering that $\sqrt{G(t)}=J_\xi^y(t)$, the Jacobian may be reformulated using the chain rule (Aris 1962, p. 145):[4]

$$J_\xi^y(t)=J_x^yJ_\xi^x(t). \tag{15}$$

So

$$\omega^\gamma=\frac{1}{J_\xi^x(t)}\frac{\epsilon^{\alpha\beta\gamma}}{J_x^y}\frac{\partial u_\beta(t_0)}{\partial\xi^\alpha}+\int_{t_0}^{t}dt'\frac{\epsilon^{\alpha\beta\gamma}}{J_\xi^y(t)}\frac{\partial f_\beta(t')}{\partial\xi^\alpha}. \tag{16}$$

Noting that

$$J_x^y=J_\xi^y(t_0), \tag{17}$$

we write

$$\omega_0^\gamma\equiv\frac{\epsilon^{\alpha\beta\gamma}}{J_\xi^y(t_0)}\frac{\partial u_\beta(t_0)}{\partial\xi^\alpha}, \tag{18}$$

which is the initial vorticity at the reference time t_0. Then,

$$\omega^\gamma(t)=\frac{\omega_0^\gamma}{J_\xi^x(t)}+\int_{t_0}^{t}dt'\frac{\epsilon^{\alpha\beta\gamma}}{J_\xi^y(t)}\frac{\partial f_\beta(t')}{\partial\xi^\alpha}. \tag{19}$$

The integrand may be rewritten noting that

$$J_\xi^y(t')=J_x^yJ_\xi^x(t'), \tag{20}$$

and thus,

$$J_x^y=\frac{J_\xi^y(t')}{J_\xi^x(t')}. \tag{21}$$

Inserting this expression for J_x^y into Eq. (15) gives

$$J_\xi^y(t)=\frac{J_\xi^x(t)}{J_\xi^x(t')}J_\xi^y(t'). \tag{22}$$

Finally, using Eq. (10),

$$J_\xi^y(t)=\frac{\rho(t')}{\rho(t)}J_\xi^y(t'). \tag{23}$$

[3] If $\mathbf{J}$ epresents the transformation matrix from the x^j coordinates to Cartesian coordinates, we know that $(\mathbf{J}\cdot\mathbf{J})_k^i=J_j^iJ_k^j$, and consequently, $(\mathbf{J}^{\mathrm{T}}\cdot\mathbf{J})_k^i=\sum_jJ_i^jJ_k^j=g_{ik}$. So, $\mathbf{J}^{\mathrm{T}}\cdot\mathbf{J}=\mathbf{g}$, which is the metric tensor, and which implies $\det(\mathbf{J}^{\mathrm{T}}\cdot\mathbf{J})=\det(\mathbf{g})$. It follows that $\det(\mathbf{J}^{\mathrm{T}}\cdot\mathbf{J})=\det(\mathbf{J}^{\mathrm{T}})\det(\mathbf{J})=\det(\mathbf{J})\det(\mathbf{J})=[\det(\mathbf{J})]^2=g$.

[4] The matrix $(\mathbf{J}_\xi^y)_\alpha^i=\partial y^i/\partial\xi^\alpha$ may be written, upon applying the chain rule, as $\partial y^i/\partial x^k\cdot\partial x^k/\partial\xi^\alpha$, which may be interpreted as the product of two matrices. Taking the determinant of a matrix product $\mathbf{A}\cdot\mathbf{B}$ gives $\det(\mathbf{A}\cdot\mathbf{B})=\det(\mathbf{A})\det(\mathbf{B})$. In symbolic notation, we may then write $J_\xi^y=\det(\partial y/\partial\xi)$, and apply the chain rule such that $\det(\partial y/\partial\xi)=\det(\partial y/\partial x)\det(\partial x/\partial\xi)$.

Substituting this in the integrand of Eq. (19) and using Eq. (10) also in the first term, gives

$$\omega^\gamma(t) = \frac{\rho(t)}{\rho(t_0)}\omega_0^\gamma + \int_{t_0}^{t} dt' \frac{\rho(t)}{\rho(t')} \frac{\epsilon^{\alpha\beta\gamma}}{J_\xi^\gamma(t')} \frac{\partial f_\beta(t')}{\partial \xi^\alpha}. \tag{24}$$

Recognizing the material torque in the integrand,

$$\tau^\gamma(t') \equiv \frac{\epsilon^{\alpha\beta\gamma}}{J_\xi^\gamma(t')} \frac{\partial f_\beta(t')}{\partial \xi^\alpha}, \tag{25}$$

we may write

$$\omega^\gamma(t) = \frac{\rho(t)}{\rho(t_0)}\omega_0^\gamma + \int_{t_0}^{t} dt' \frac{\rho(t)}{\rho(t')} \tau^\gamma(t'). \tag{26}$$

This is the vorticity in the material frame, and this formulation affords an interesting interpretation of the vorticity parts. In the deformed material frame, there is a contribution from the initial vorticity, which only changes as the volume is expanded or compressed between t_0 and t (here referred to as expansion/compression effect), which is schematically shown in Fig. 1. This effect can be understood by recognizing that the vorticity within a vortex tube increases if the tube's cross-sectional area decreases. Assume that the ξ^γ axis is parallel to the vortex tube. If the volume of the fluid element, e.g., decreases, but such that the cross-sectional area normal to the vortex tube remains constant, then the material axis parallel to the vortex tube is compressed, and accordingly the material vorticity component along this axis increases (Fig. 1b). On the other hand, if the cross-sectional area normal to the vortex tube, e.g., decreases but the material axis parallel to the vortex tube remains unchanged, the vorticity component along this axis will increase because of angular momentum conservation (Fig. 1c). Thus, this effect describes the "nonfrozenness" of this vorticity part in nonisochoric flows. Finally, if the volume remains constant, the magnitude of the vorticity vector may still change but then the vector is frozen into the material frame and the vorticity components along the material axes remain constant (Fig. 1d).

The second part of Eq. (26) describes the effect of the torques due to nonconservative forces acting on the flow, taking into account the incremental expansion/compression effect. In essence, this part is the integral of the material torque. In this analysis, the torque includes the baroclinic vorticity production, vorticity generated via SGS and numerical mixing, as well as curl of the Coriolis force.

Except for the compression/expansion effect in nonisochoric flows, the material description does not include tilting and stretching of the vorticity vector, which is related to the deformation of the fluid volume. This deformation is implicitly included in the material description. These effects appear explicitly if the coordinates are changed to the fixed spatial frame using the vector transformation law:

$$\omega^i(t) = \frac{\partial x^i}{\partial \xi^\gamma}(t)\left[\frac{\rho(t)}{\rho(t_0)}\omega_0^\gamma + \int_{t_0}^{t} dt' \frac{\rho(t)}{\rho(t')}\tau^\gamma(t')\right]. \tag{27}$$

If the torque in the integrand is zero, the equation recovers Cauchy's vorticity formula (e.g., Truesdell 1954; Dutton 1976; Davies-Jones 2000; Dahl et al. 2014). Note that Eq. (27), giving the spatial components of the vorticity vector, still pertains to individual parcels. However, rather than considering the projection of the vorticity parts onto the time-dependent material coordinate basis [Eq. (26)], we now consider the projections onto the fixed spatial coordinate basis (which is usually represented by the standard Cartesian basis).

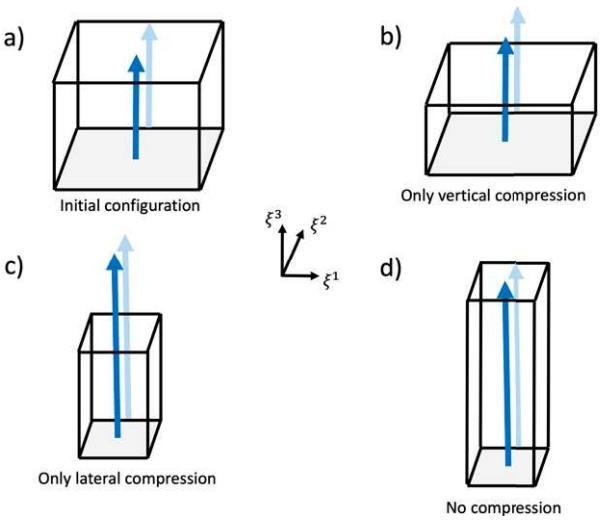

FIG. 1. Qualitative depiction of the compression/expansion effect. The dark-blue arrow represents the vorticity vector, and the light-blue vector is the projection of this vector on the sidewall of the material volume. (a) Initial configuration; (b) vertical compression leaves the horizontal cross-sectional area as well as the vorticity vector unchanged, but the material vertical vorticity component increases; (c) lateral compression leads to an increase of the vorticity vector as well as its vertical material component due to horizontal convergence; (d) the volume is isochorically deformed and the vorticity vector lengthens due to horizontal convergence, but its vertical material component remains unchanged.

The torque in Eq. (27) is given in material coordinates and may be cumbersome to calculate using, e.g., model output or observational data. However, after a coordinate transformation, the spatial components of the torque appear:

$$\tau^\gamma(t') = \frac{\partial \xi^\gamma}{\partial x^j}(t')\tau^j(t'). \tag{28}$$

The final version of Eq. (27) then becomes

$$\omega^i(t) = \frac{\partial x^i}{\partial \xi^\gamma}(t)\left[\frac{\rho(t)}{\rho(t_0)}\omega_0^\gamma + \int_{t_0}^{t} dt' \frac{\rho(t)}{\rho(t')}\frac{\partial \xi^\gamma}{\partial x^j}(t')\tau^j(t')\right]. \tag{29}$$

In symbolic form, Eq. (29) reads

$$\boldsymbol{\omega}^\gamma = \frac{\partial \mathbf{r}}{\partial \boldsymbol{\xi}}(t)\cdot\left[\frac{\rho(t)}{\rho(t_0)}\boldsymbol{\omega}_0 + \int_{t_0}^{t} dt' \frac{\rho(t)}{\rho(t')}\frac{\partial \boldsymbol{\xi}}{\partial \mathbf{r}}(t')\cdot\boldsymbol{\tau}(t')\right]. \tag{30}$$

This is the (slightly reformulated) "not inelegant" basic vorticity formula by Truesdell (1954, p. 154). By writing out each of the two terms separately and explicitly considering all contributions to $\boldsymbol{\tau}$, the vorticity source decomposition is obtained:

$$\omega_P^i(t) = \frac{\partial x^i}{\partial \xi^\gamma}(t)\frac{\rho(t)}{\rho(t_0)}\omega_0^\gamma, \tag{31}$$

$$\omega_N^i(t) = \frac{\partial x^i}{\partial \xi^\gamma}(t)\left[\int_{t_0}^{t} dt' \frac{\rho(t)}{\rho(t')}\frac{\partial \xi^\gamma}{\partial x^j}(t')\tau_N^j(t')\right], \tag{32}$$

where the subscripts describe the sources of the vorticity that is subsequently rearranged. Here, P stands for "preexisting" and $N \in \{\text{BC, SGS, DIFF, COR}\}$, is a placeholder describing the different torques:

$$\boldsymbol{\tau}_{\text{BC}} = \boldsymbol{\nabla} \times \left(-\frac{1}{\rho}\boldsymbol{\nabla} p\right), \tag{33}$$

$$\boldsymbol{\tau}_{\text{SGS}} = \boldsymbol{\nabla} \times \mathbf{f}_{\text{sgs}}, \tag{34}$$

$$\boldsymbol{\tau}_{\text{DIFF}} = \boldsymbol{\nabla} \times \mathbf{f}_{\text{diff}}, \tag{35}$$

$$\boldsymbol{\tau}_{\text{COR}} = \boldsymbol{\nabla} \times (-f\mathbf{k} \times \mathbf{v}_h'). \tag{36}$$

The meaning of the subscripts as well as the interpretation of the different vorticity parts are discussed in the next subsection. Equations (31) and (32) are, respectively, equivalent to Eqs. (33) and (36) by Davies-Jones (2022). The initial conditions for $\boldsymbol{\omega}_P$ and $\boldsymbol{\omega}_N$ immediately follow from Eqs. (31) and (32):

$$\boldsymbol{\omega}_P(t_0) = \boldsymbol{\omega}(t_0), \tag{37}$$

and

$$\boldsymbol{\omega}_{\text{BC}}(t_0) = \boldsymbol{\omega}_{\text{SGS}}(t_0) = \boldsymbol{\omega}_{\text{DIFF}}(t_0) = \boldsymbol{\omega}_{\text{COR}}(t_0) = \mathbf{0}. \tag{38}$$

Implementation of the vorticity source decomposition

As shown in appendix A, Truesdell's vorticity formula, Eq. (29), leads to this form of the partial vorticity equations,

$$\frac{d\boldsymbol{\omega}_N}{dt} = \boldsymbol{\omega}_N \cdot \boldsymbol{\nabla}\mathbf{v} - \boldsymbol{\omega}_N(\boldsymbol{\nabla} \cdot \mathbf{v}) + \boldsymbol{\tau}_N, \tag{39}$$

where now the placeholder $N \in \{P, \text{BC, SGS, DIFF, COR}\}$ includes the preexisting part with

$$\boldsymbol{\tau}_P = \mathbf{0}. \tag{40}$$

Additional torque terms could be used as needed, such as the torque associated with gradients in hydrometeor load (e.g., Davies-Jones 2022). Equations corresponding to Eq. (39) appeared in Davies-Jones [2006; his Eqs. (5.1)–(5.4)], and for incompressible flows, in the analyses by, e.g., Epifanio and Durran (2002) and Markowski (2016). The vorticity parts are given by the integral of Eq. (39) for each N:

$$\boldsymbol{\omega}_P(t) = \boldsymbol{\omega}(t_0) + \int_{t_0}^{t} dt'[\boldsymbol{\omega}_P(t') \cdot \boldsymbol{\nabla}\mathbf{v}(t') - \boldsymbol{\omega}_P(t')\boldsymbol{\nabla} \cdot \mathbf{v}(t')], \tag{41}$$

$$\boldsymbol{\omega}_{\text{BC}}(t) = \int_{t_0}^{t} dt'[\boldsymbol{\omega}_{\text{BC}}(t') \cdot \boldsymbol{\nabla}\mathbf{v}(t') - \boldsymbol{\omega}_{\text{BC}}(t')\boldsymbol{\nabla} \cdot \mathbf{v}(t') + \boldsymbol{\tau}_{\text{BC}}(t')], \tag{42}$$

$$\boldsymbol{\omega}_{\text{SGS}}(t) = \int_{t_0}^{t} dt'[\boldsymbol{\omega}_{\text{SGS}}(t') \cdot \boldsymbol{\nabla}\mathbf{v}(t') - \boldsymbol{\omega}_{\text{SGS}}(t')\boldsymbol{\nabla} \cdot \mathbf{v}(t') + \boldsymbol{\tau}_{\text{SGS}}(t')], \tag{43}$$

$$\boldsymbol{\omega}_{\text{DIFF}}(t) = \int_{t_0}^{t} dt'[\boldsymbol{\omega}_{\text{DIFF}}(t') \cdot \boldsymbol{\nabla}\mathbf{v}(t') - \boldsymbol{\omega}_{\text{DIFF}}(t')\boldsymbol{\nabla} \cdot \mathbf{v}(t') + \boldsymbol{\tau}_{\text{DIFF}}(t')], \tag{44}$$

$$\boldsymbol{\omega}_{\text{COR}}(t) = \int_{t_0}^{t} dt'[\boldsymbol{\omega}_{\text{COR}}(t') \cdot \boldsymbol{\nabla}\mathbf{v}(t') - \boldsymbol{\omega}_{\text{COR}}(t')\boldsymbol{\nabla} \cdot \mathbf{v}(t') + \boldsymbol{\tau}_{\text{COR}}(t')]. \tag{45}$$

The first part represents the effect of tilting and stretching of the initial or preexisting vorticity, and it represents the vorticity imported into the supercell from the environment. This vorticity part is commonly called "barotropic" vorticity, a designation apparently first introduced by Dutton (1976, p. 389) for inviscid flows. However, this designation seems misleading if mixing is included, which is why we use the term "preexisting" vorticity.[5] The second part is the baroclinically produced, and subsequently rearranged vorticity, which is referred to as baroclinic vorticity (suffix "BC"). This part is zero initially and thus includes the total effect of baroclinic production. For example, a small amount of baroclinic production may lead to initially insignificant vorticity, but upon strong stretching this vorticity may dominate the flow after some time. In the traditional picture, the stretching term would dominate, but in the source decomposition, the baroclinity would be highlighted as ultimate dynamical source of the vorticity. Finally, there is the vorticity that has been produced by SGS mixing and numerical diffusion (DIFF), and which has subsequently been rearranged. Numerical diffusion is also referred to as implicit diffusion or implicit mixing, and it is present when odd-ordered advection schemes are used (e.g., Wicker and Skamarock 2002), as is the case in the present simulation. That is, the odd-ordered advection scheme has a built-in noise

[5] Consider an inviscid fluid, in which one may always define a preexisting vorticity part that behaves as if the flow were barotropic, hence the designation "barotropic vorticity." The remaining vorticity part is newly generated via baroclinity and then rearranged, which is the baroclinic vorticity. However, in barotropic flows with nonzero (molecular, eddy, or computational) mixing, the designation is perhaps misleading because now there is a barotropic part (preexisting vorticity being rearranged) and a "nonbarotropic" part that is caused by viscous effects. There would thus be nonbarotropic vorticity even though the flow is purely barotropic. Moreover, this nomenclature has led several authors to refer to the rearrangement of preexisting vortex lines as a "barotropic" process (e.g., Davies-Jones 2008; Markowski 2016; Dahl 2017), which in most cases is misleading because horizontal gradients in vertical motion in convective storms are often associated with horizontal buoyancy gradients, i.e., baroclinity.

filter. The SGS mixing term is especially large near the surface where it describes the effect of surface drag (e.g., Markowski and Bryan 2016).

The vorticity source decomposition offers different insights into the vorticity dynamics than the traditional formulation. Aside from the effect just described, whereby a small amount of vorticity production may be identified as dynamically important, the impact of the initial, or preexisting, vorticity can be quantified. If the initial vorticity closely corresponds to the base-state vorticity, the direct contribution of imported ambient vorticity to the rotation of the tornado can be assessed. A practical disadvantage of this vorticity source decomposition is that the vorticity parts in the integrands are not known along the trajectory and they must be calculated using an iterative or an implicit scheme (appendix B). Unfortunately, this integration is prone to error growth, and matching vorticity budgets are less likely to be achieved than for traditional budgets. While Markowski (2016) attributed most of the error growth to the nonlinear advection, in our case this is related to the fact that the tilting and stretching terms are calculated using the partial vorticity obtained from the previous integration steps (in the "traditional" integration, one uses the known interpolated vorticity components, so the problem is not as severe). This effect is aggravated near the vortex where large velocity gradients exist, so that the errors rapidly escalate. To alleviate these errors, we used trajectory data output on every large model time step (0.5 s). The trajectory data were calculated during runtime within CM1 on their respective staggered grids, and then interpolated trilinearly to the parcel locations. When integrating the vorticity budgets several solvers were tested to mitigate error growth (including those available in the Python library solve_ivp as well as manually implemented Runge–Kutta and implicit schemes). While all solution methods yielded the same results, the implicit scheme (appendix B) was most efficient computationally.[6] Despite the efforts to maximize trajectory accuracy, as well as accuracy when calculating the forcing terms, only for a small number of parcels ($n = 7$; see section 2) were the integrals of sufficient quality to warrant further analysis.

4. Results

Figure 2 shows the tornado-like vortex at the lowest scalar model level (Fig. 2a), along with the vertical motion field at 250 m AGL. Besides the main cyclonic vortex, a weaker anticyclonic vortex is also present, and there is a downdraft between the vortices and southwest of the main (cyclonic) vortex. These downdrafts are likely forced by dynamic pressure gradient accelerations (e.g., Klemp and Rotunno 1983; Schenkman et al. 2016). Northwest of the main vortex there is a rather stationary internal boundary as revealed by the horizontal wind-vector convergence, which is accompanied by a tongue of rising motion northwest of the TLV. This boundary and the associated region of upward motion persisted throughout the TLV's lifetime. As will be seen, these vertical motion regimes are critical in shaping the parcel trajectories as they approach the main vortex.

Figure 2b shows a vertical (south–north) cross section through the center of the cyclonic vortex. Although the vertical vorticity in the vortex core does not exhibit an annular structure, a two-celled structure is apparent in the flow field, with downflow in the central vortex portions and an annular corner-like flow surrounding it. The upward velocity at the southern vortex periphery exceeds 40 m s^{-1} at about 1 km AGL. The vortex formed around 3000 s simulation time and persisted through the end of the simulation at 5400 s.

a. Trajectory overview

The seven trajectories based on the storm-relative wind are shown as black line segments in Fig. 3 and are seen to enter the TLV. The vast majority of the trajectories originating from the north/northeast of the vortex descend below the lowest scalar model level or had poorly matching budgets and were not considered. The focus is thus on the airstream originating east of the mesocyclone. While parcels with similar trajectories have been identified in previous studies (e.g., Wicker and Wilhelmson 1995; Markowski and Richardson 2014; Dahl et al. 2014; Mashiko 2016; Boyer and Dahl 2020), in the present case the descent in the forward flank region is rather gentle, and the parcels do not yet reach the surface. Instead, they rise again as they traverse the tongue of rising motion northwest of the main TLV discussed in the previous paragraph. The parcels subsequently descend comparatively quickly close to the surface in the occlusion downdraft before they enter the TLV [as was also observed by, e.g., Schenkman et al. (2014) and Mashiko (2016)].

Before analyzing the vorticity dynamics in detail, the vertical vorticity parts of the parcels as they enter the base of the vortex, obtained by integrating Eqs. (41)–(45) along each of the seven trajectories, are shown in Fig. 4. Parcel A is represented in blue, and parcel B in red. Notably, for all parcels the vertical vorticity is dominated by the SGS part caused mainly by surface drag [even for parcel A (blue dots), ζ_{SGS} becomes slightly positive as the parcel rises in the vortex]. The ζ_P and ζ_{BC} parts contribute positively only for some parcels. Interestingly, for the parcels analyzed here, when the imported part is positive, the baroclinic part is negative, and vice versa. The part due to numerical mixing ζ_{DIFF} also makes a net positive contribution to the vorticity budgets and will be analyzed separately in section 5b. Finally, the contribution due to the Coriolis force (rearrangement of planetary vorticity) is generally small and will not be discussed in the subsequent analysis. In the following we will consider two representative parcels for which either the imported or the baroclinic vertical vorticity dominates at the base of the TLV.

b. Parcel A

First, we consider parcel A (Fig. 3). Before presenting the vorticity source decomposition, the results of the traditional integration of the vorticity equation, Eqs. (2)–(6), will be

[6] Note that the data required along the trajectory are the same for the traditional integration as for the vorticity source decomposition.

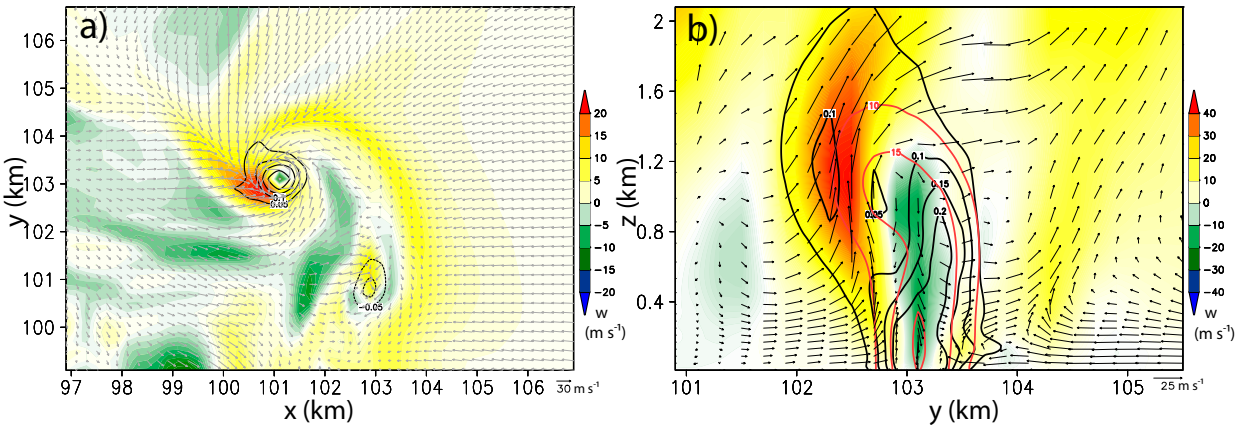

FIG. 2. (a) Vertical velocity at 250 m AGL (shaded), horizontal storm-relative wind vectors at 10 m AGL, and vertical vorticity at 10 m AGL [contours, (−0.1, −0.05, 0.05, 0.1, 0.15, 0.2) s^{-1}]. (b) South–north cross section through the vortex at x = 101.1 km. Vertical motion is shaded, the red contours represent the pressure perturbation (hPa), and the black contours represent vertical vorticity (s^{-1}). The velocity vectors in the (y, z) plane are also shown (black arrows). Both fields are shown at 4020 s simulation time.

shown separately for the horizontal vorticity magnitude and the vertical vorticity component. The contributions to the horizontal vorticity magnitude are displayed in two different ways: (i) by calculating the magnitudes due to each contribution separately (e.g., $\omega_h^{bc} = \sqrt{\xi_{bc}^2 + \eta_{bc}^2}$), shown in Fig. 5a. Because the different contributions are generally not parallel to one another, their sum does not add up to the total horizontal vorticity magnitude; (ii) by calculating the projection of each integrated horizontal vorticity contribution onto the horizontal vorticity vector, which follows from the equation for the horizontal vorticity magnitude (e.g., Boyer and Dahl 2020), $d|\boldsymbol{\omega}_h|/dt = \mathbf{s}\cdot\dot{\boldsymbol{\omega}}_h$, where $\mathbf{s} = \boldsymbol{\omega}_h/|\boldsymbol{\omega}_h|$ is the unit vector parallel to the horizontal vorticity. This is shown in Fig. 5b.

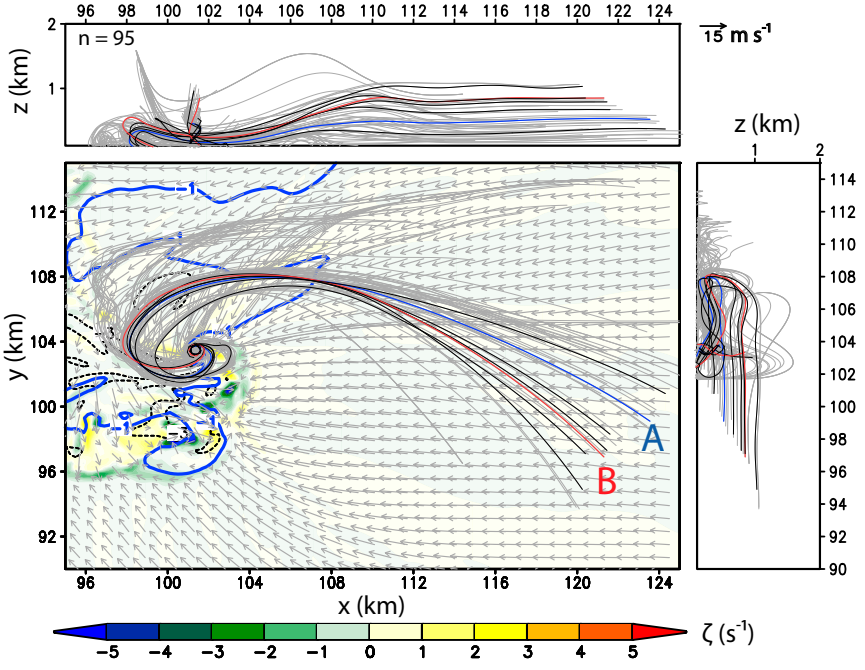

FIG. 3. Overview of the trajectories analyzed in this study, spanning the time interval [2400, 4200] s. The blue and red trajectories (labeled A and B, respectively) pertain to the two parcels analyzed in detail, and the black trajectories represent the seven analyzed parcels. The gray line segments show all remaining 88 trajectories, including many that descended below the lowest scalar model level or otherwise did not qualify for analysis. The vorticity field (shaded), the storm-relative wind field (vectors), and the −1 K potential temperature perturbation contour (blue line) are shown at 10 m AGL and 4200 s.

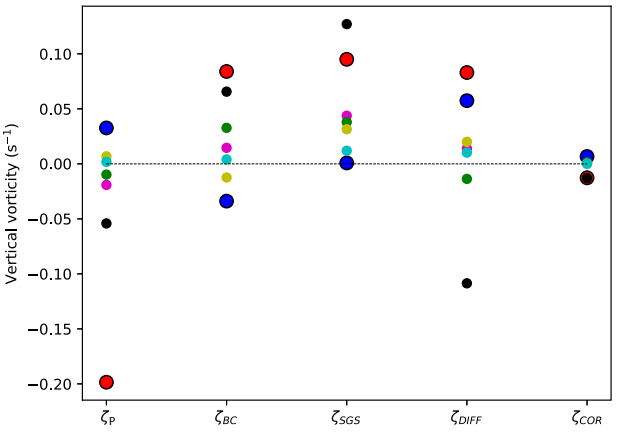

FIG. 4. Vertical vorticity (ζ) parts at the moment the parcels commence their ascent as they enter the vortex. Each color uniquely corresponds to one parcel. Parcel A is represented by blue dots, and parcel B by red dots.

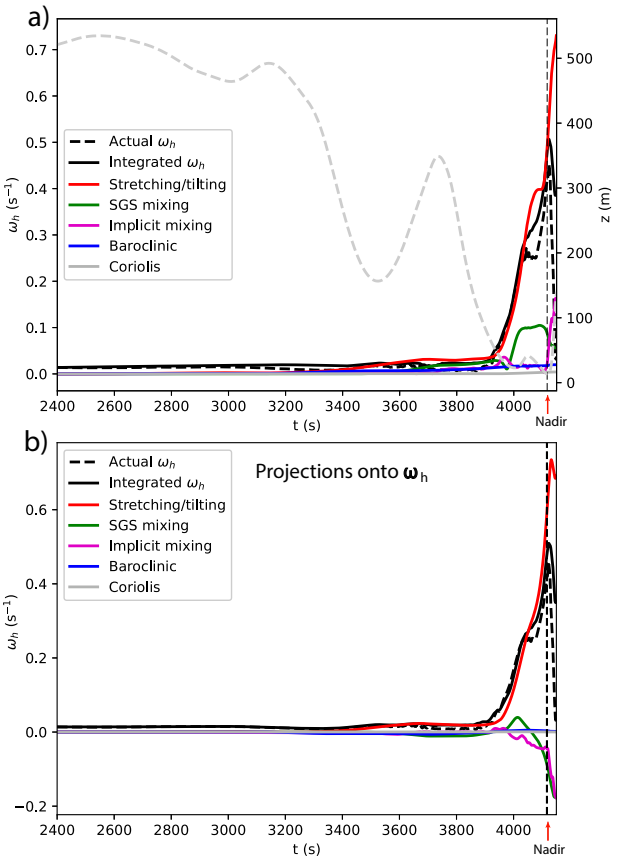

FIG. 5. Time series of (a) the horizontal vorticity magnitudes based on the different integrated terms in the traditional vorticity equation for parcel A. The parcel height is shown as gray dashed line. (b) Integrated projection onto the horizontal vorticity vector of the individual terms of the traditional horizontal vorticity equation for parcel A.

The analysis reveals that the horizontal vorticity magnitude is dominated by horizontal stretching as the parcels accelerate toward the vortex (Fig. 5a). There are relatively large contributions from the SGS mixing terms after about 4000 s, which however are oriented such that the horizontal vorticity magnitude decreases somewhat. This is seen in Fig. 5b, which shows the projection of each integrated horizontal vorticity contribution onto the horizontal vorticity vector.

Notably, there is practically (but not perfectly) zero baroclinic production of horizontal vorticity along the parcel's 30 min history. What little baroclinic vorticity production the parcel experiences occurs in the forward flank region of the storm, where there are weak horizontal buoyancy gradients (Fig. 6). Notably, but perhaps not unexpectedly, no appreciable horizontal vorticity is generated baroclinically as the parcels descend through the occlusion downdraft.[7]

The vertical vorticity budget, shown in Fig. 7 is dominated by the tilting and stretching terms, as well as by implicit diffusion. It is seen that the tilting and numerical diffusion contributions increase as the parcel reaches its nadir (at about 13 m AGL), leading to an increase in vertical vorticity. Subsequently, the stretching term, acting on that vertical vorticity, leads to a rapid increase of vertical vorticity as the parcel enters, and rises within, the vortex. This progression is consistent with the "in-and-up" mechanism (Boyer and Dahl 2020; Fischer and Dahl 2022) augmented by diffusion.

Perhaps surprisingly, when considering the vorticity source decomposition (Fig. 8) the seemingly negligible amount of baroclinically produced vorticity is subject to significant stretching, such that the baroclinic vorticity becomes a dominant source in terms of vorticity magnitude. Another significant contribution comes from the imported vorticity. However, as seen in Figs. 8a and 8b, the two vorticity parts point in opposite directions. The $\boldsymbol{\omega}_P$ part contributes positively to the vertical vorticity, while the baroclinic part contributes negatively. That is, the imported vorticity directly helps maintain the rotation of the TLV via abrupt upward tilting as the parcel enters the TLV. The vorticity due to SGS mixing remains horizontal as the parcel enters the vortex, and thus does not contribute to the vertical vorticity of the parcel (only a bit later the SGS vorticity attains a positive vertical component as the air continues to rise). The diffusive vertical vorticity contributes the most, but as will be discussed in section 5b, this effect does not contribute to vortex maintenance. Figure 8 only affords a qualitative picture of the relative magnitudes and general orientations of the different vorticity parts. To quantify the different vorticity parts, Fig. 9 shows the individual horizontal vorticity magnitudes as well as the vertical vorticity, highlighting the diffusive and preexisting (imported) parts as the dominant contributors.

c. *Parcel B*

The traditional integrals for parcel B (Fig. 3) reveal a similar evolution as was found for parcel A. When considering the

[7] The perturbation pressure gradient accelerations are approximately irrotational, and consequently cannot generate vorticity.

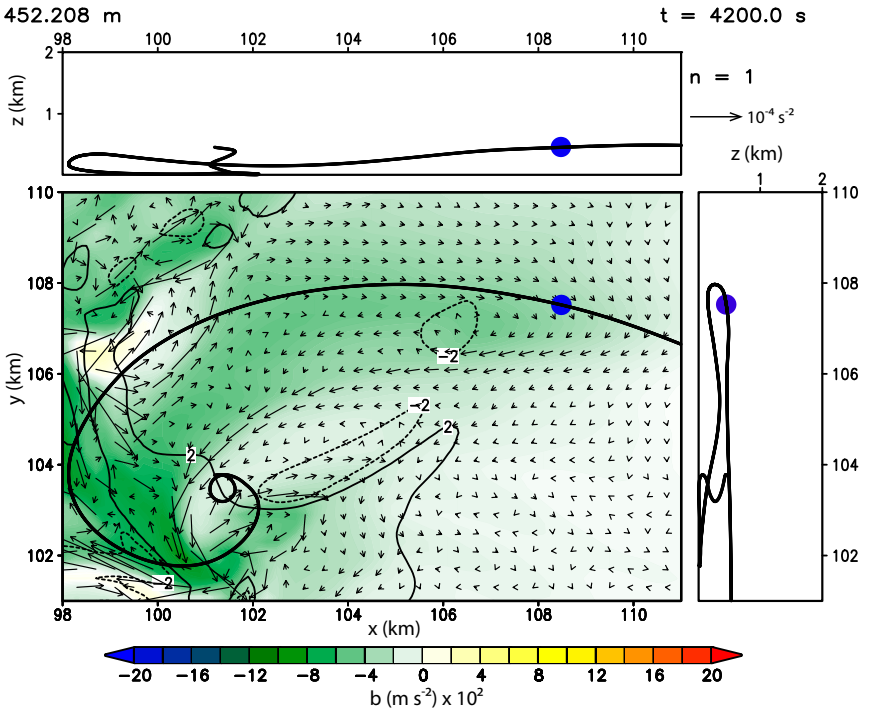

FIG. 6. Buoyancy field as well as baroclinic vorticity production at 452 m AGL and 3240 s. The location of parcel A pertaining to the level and time shown is marked as a blue circle.

magnitudes of the horizontal vorticity contributions using the traditional integral, shown in Fig. 10a, the dominant terms are again the tilting/stretching terms as the parcel accelerates toward the vortex, entering it about 20 m AGL. The magnitude of the integrated baroclinic production is nonzero, but this contribution has a component in the opposite direction of the horizontal vorticity vector, implying that it tends to reduce the horizontal vorticity magnitude. This is inferred from the projections of the horizontal vorticity contributions onto the horizontal vorticity vector, shown in Fig. 10b. Likewise, implicit mixing again contributes negatively, but in contrast to parcel A, SGS mixing leads to an increase of horizontal vorticity magnitude due to surface drag.

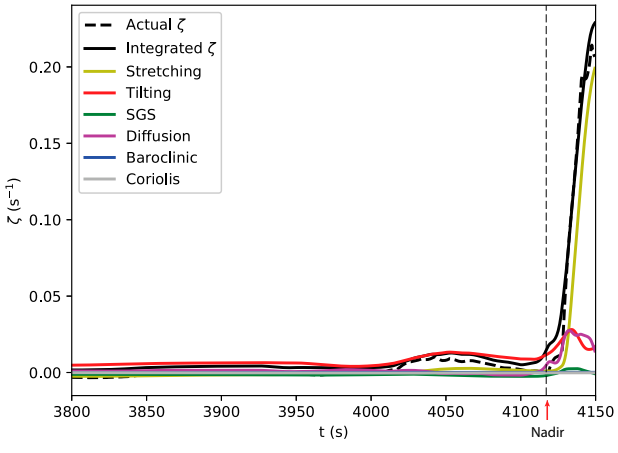

FIG. 7. Vertical vorticity budgets using the traditional vorticity integral for parcel A. Here, diffusion refers to implicit (numerical) mixing.

The vertical vorticity budget, shown in Fig. 11, likewise resembles that of parcel A. First the vertical vorticity due to tilting increases, and this vorticity is subsequently stretched vertically as the parcel rises in the updraft. The effect of implicit diffusion also contributes to an increase in vertical vorticity, as for the other parcel. In short, the traditional vorticity budgets are quite similar for both parcels.

The source decomposition reveals rather large differences in the vorticity dynamics of parcel B compared to parcel A. As shown in Fig. 12, both the imported and baroclinic vorticity vectors along trajectory B become oriented oppositely to the corresponding vectors along trajectory A. That is, the imported preexisting vorticity attains a downward component, while the baroclinic vorticity points upward, which thereby contributes positively to the rotation of the TLV. This is also seen in the time evolution of the different vorticity parts displayed in Fig. 13. Moreover, the SGS vorticity, caused mainly by surface drag is abruptly tilted upward at the base of the vortex, as also recognized by Schenkman et al. (2014), Roberts et al. (2016), and Roberts and Xue (2017).

In summary, while the analysis of the traditional vorticity equation suggests that both parcels behave rather similarly to one another, the vorticity source decomposition reveals stark differences in the relative contributions of imported and baroclinic vorticity. These differences are explored in the next section.

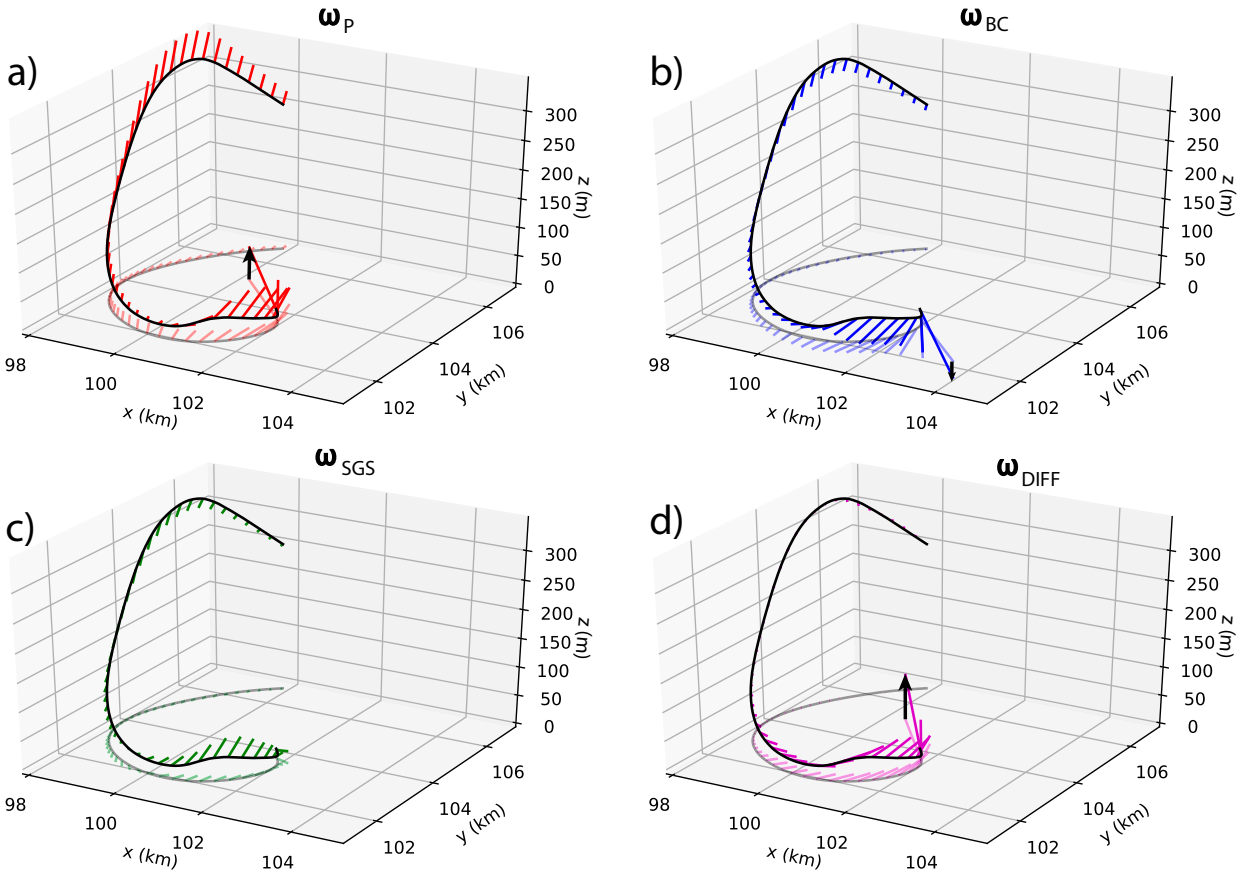

FIG. 8. Qualitative 3D depiction of the vorticity source decomposition, with (a) imported preexisting vorticity $\boldsymbol{\omega}_P$, (b) baroclinic vorticity $\boldsymbol{\omega}_{BC}$, (c) SGS vorticity $\boldsymbol{\omega}_{SGS}$, and (d) diffusive vorticity $\boldsymbol{\omega}_{DIFF}$ of parcel A. The vorticity vectors are represented by line segments originating from the trajectory (black line). The black arrows indicate the direction of the vertical vorticity vector at the end of the time interval for which the trajectory is displayed, [3550, 4125] s.

5. Discussion

a. *Difference in behavior of imported and baroclinic vorticity between trajectories A and B*

An interesting observation in the analysis is that, while the traditional vorticity budgets pointed to rather similar vorticity dynamics, the vorticity source decomposition yielded large differences between parcels A and B in the configuration of both the baroclinic and imported vorticity vectors. While the vorticity vectors (either imported or baroclinic) are initially aligned similarly, they are imbedded in different strain fields, which is in part related to the inhomogeneous downdraft field these parcels pass through (Fig. 14). To see the differences in the strain field along the trajectories, the principal axes of the local strain tensor corresponding to the intermediate eigenvalues are shown in Fig. 15, along with the imported vorticity. The eigenvectors were calculated following Kundu and Cohen (2008, p. 41). The orientation of the eigenvectors corresponds to the axes of deformation. Although one might expect the vorticity vectors to become aligned with the eigenvector associated with the largest positive eigenvalue, which signifies the direction of maximum stretching (Hamlington et al. 2008), it has long been recognized that the vorticity vectors tend to become aligned with the intermediate axis of deformation of the rate-of-strain tensor (e.g., Hamlington et al. 2008; Coriton and Frank 2016). Hamlington et al. (2008) explain this behavior with the strain induced by the local vortex structure itself, which often exceeds the background strain that reoriented and stretched the vortex in the first place. As can be seen in Fig. 15, the imported vorticity has a different alignment for each parcel relative to the deformation axis, indicating that the vorticity vectors along each trajectory will be reoriented in a different fashion, ultimately resulting in opposite orientations of the vectors for each parcel. The final alignment approaches the intermediate deformation axis (Hamlington et al. 2008).

The result is that all vorticity parts tend to become oriented approximately parallel or antiparallel to one another, as is also apparent in the analysis by Dahl et al. (2014) and Dahl (2015). This implies that even in the presence of the source terms, influencing the vorticity evolution for all but the imported vorticity parts, the deformation effect (tilting/stretching) dominates over those sources. That is, the tendency to become aligned with the intermediate deformation axis is not affected much by the production of new vorticity, which would not in general be aligned with the intermediate deformation axis.

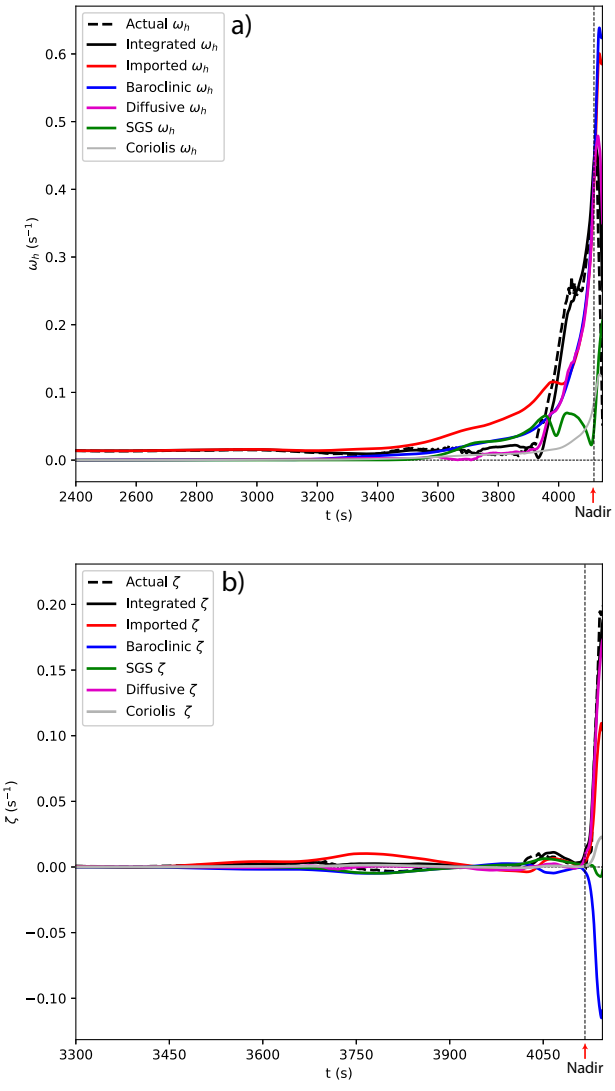

FIG. 9. Time evolution of the different vorticity parts based on the source decomposition along the trajectory of parcel A. (a) Horizontal vorticity magnitudes of the different vorticity parts; (b) vertical vorticity parts. Note the different time intervals in each panel.

b. *Role of implicit diffusion*

Many parcels experience an increase in vertical vorticity via implicit diffusion as they enter the vortex (e.g., Fig. 7; see also Markowski et al. 2014; Schenkman et al. 2014; Boyer and Dahl 2020; Fischer and Dahl 2022). To understand this contribution, consider the well-known Burgers–Rott vortex solution. Here, the azimuthal velocity is given by (e.g., Markowski and Richardson 2010)

$$v(r) = \frac{\Gamma}{2\pi r}\left[1 - \exp\left(-\frac{\alpha}{2\nu}r^2\right)\right], \tag{46}$$

where $v(r)$ is the azimuthal velocity, α is half the horizontal convergence, ν is the kinematic viscosity, Γ is the circulation.

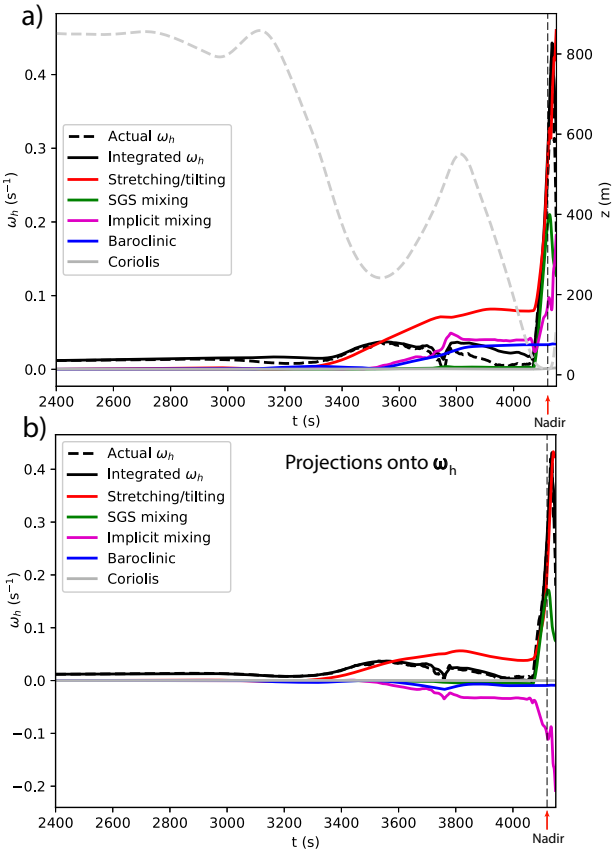

FIG. 10. As in Fig. 5, but for parcel B.

The radial velocity in the Burgers–Rott model is given by $u = -\alpha r$. With this, the vertical vorticity is found to be

$$\zeta = \frac{\partial v}{\partial r} + \frac{v}{r} = \frac{\Gamma\alpha}{2\pi\nu}\exp\left(-\frac{\alpha}{2\nu}r^2\right). \tag{47}$$

There is no horizontal vorticity in the Burgers–Rott model. Now, following the parcel motion with $r = r(t) = r_0\exp(-\alpha t)$ (via integration of $u = -\alpha r$), one obtains the vorticity tendency along a trajectory:

$$\frac{d\zeta}{dt}(t) = -\frac{\Gamma\alpha^2}{2\pi\nu^2}r(t)u(t)\exp\left[-\frac{\alpha}{2\nu}r(t)^2\right]. \tag{48}$$

To see by which mechanisms this vertical vorticity evolves along a trajectory for $r(t) > 0$, we may consider the vertical vorticity equation, which due to the symmetry of the problem, reduces to

$$\frac{d\zeta}{dt}(t) = -\zeta(t)\nabla_h \cdot \mathbf{v}_h(t) + \nu\nabla^2\zeta(t). \tag{49}$$

Now, because in this model

$$\nabla_h \cdot \mathbf{v}_h = \frac{du}{dr} + \frac{u}{r} \tag{50}$$

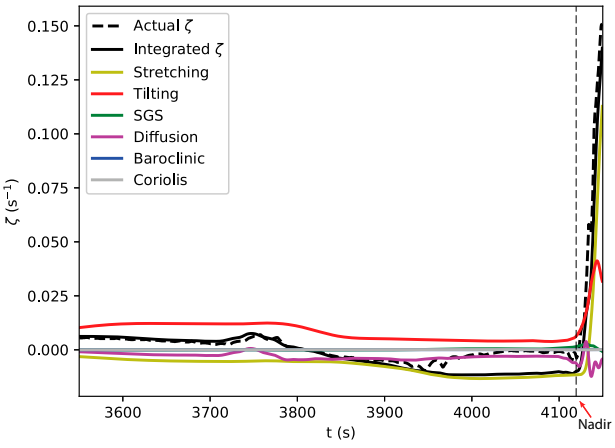

FIG. 11. As in Fig. 7, but for parcel B.

and

$$\nabla^2 = \frac{1}{r}\frac{d}{dr} + \frac{d^2}{dr^2}, \tag{51}$$

the vertical vorticity equation becomes

$$\frac{d\zeta}{dt}(t) = 2\alpha\zeta(t) + \frac{\alpha^2\Gamma}{2\pi\nu}\left[\frac{\alpha r(t)^2}{\nu} - 2\right]\exp\left[-\frac{\alpha}{2\nu}r(t)^2\right]. \tag{52}$$

The first term is the stretching term, which requires vertical vorticity to be nonzero in order to be active, and the second term describes vorticity acquisition via diffusion, which is the only vorticity source in the Burgers–Rott model. From the perspective of the vorticity source decomposition, the only nonzero part at $r > 0$ would be $\boldsymbol{\omega}_{\mathrm{DIFF}} = \zeta_{\mathrm{DIFF}}\mathbf{k}$, which is directed upward everywhere.

The terms in Eq. (52) may be integrated numerically to see how parcels acquire their vertical vorticity as they enter the vortex. Figure 16 shows that parcels first gain vertical vorticity via diffusion, whereupon this vorticity is strongly stretched vertically. This increase of vertical vorticity via diffusion is also evident in the vorticity budgets discussed above (Figs. 7 and 11). Because all parcels in the Burgers–Rott solution acquire their vertical vorticity via diffusion, one might conclude that the vortex core is maintained by diffusion. However, to obtain the steady vortex solution some initial vertical vorticity must have been present that subsequently has been concentrated. In the steady state, this initial vorticity resides at $r = 0$. Given the free-slip lower boundary in the Burgers–Rott model, the parcels initially at $z = 0$ remain there while parcels at $z > 0$ rise. The result is continued vertical stretching of their initial vertical vorticity at $r = 0$. It is this stretched initial vorticity that maintains the vortex. This stretching effect alone

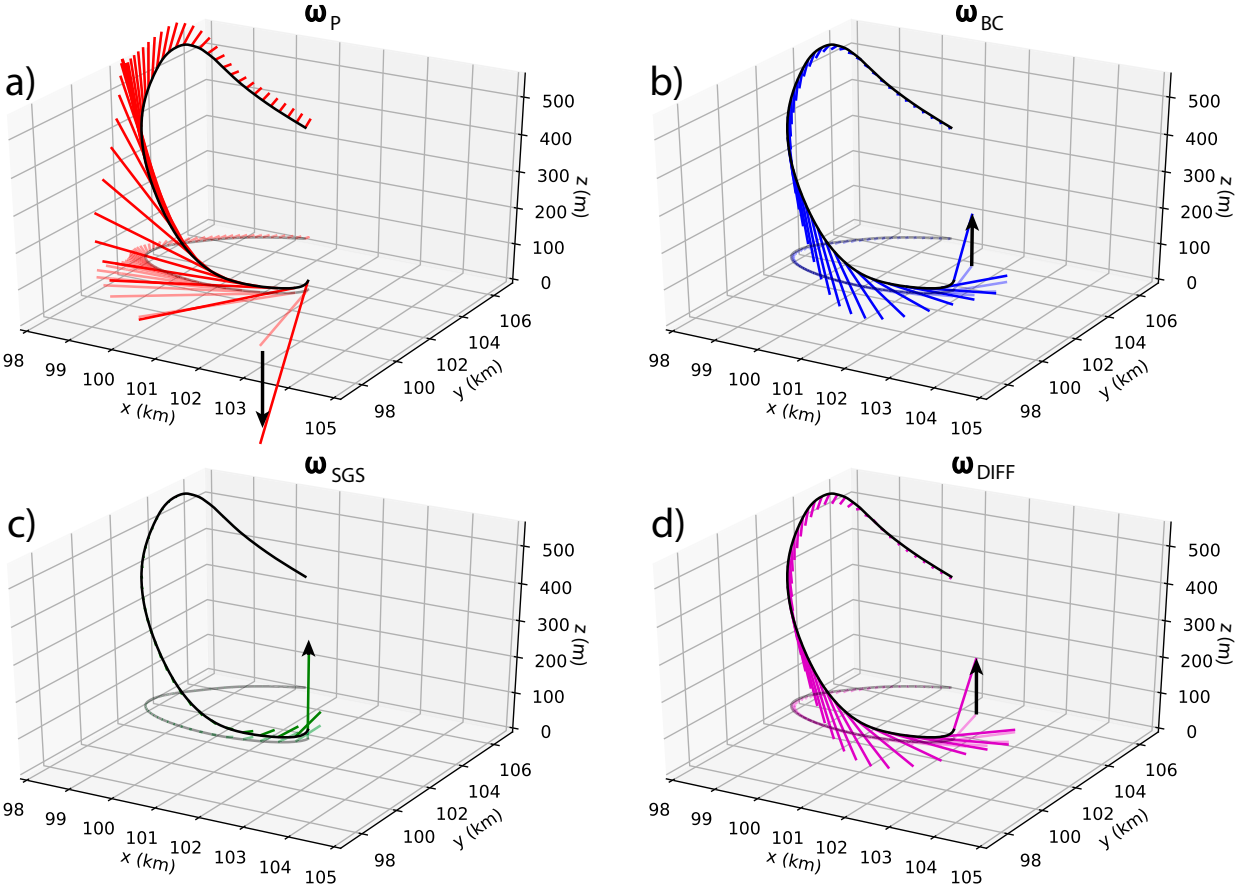

FIG. 12. As in Fig. 8, but for parcel B. Here, the time interval spans [3650, 4135] s.

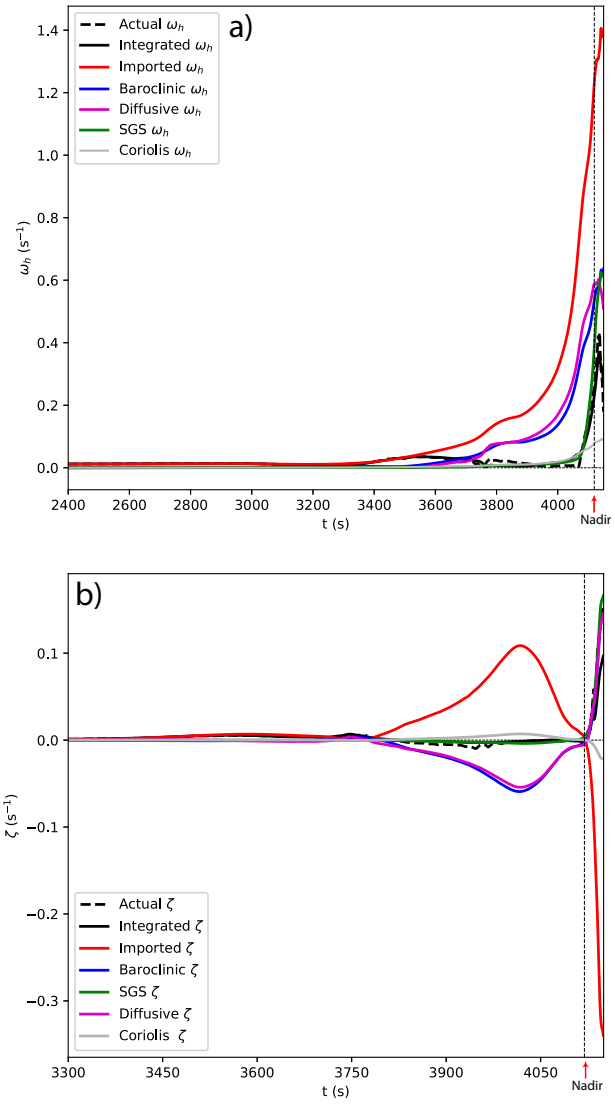

FIG. 13. Time evolution of the different vorticity parts based on the source decomposition along the trajectory of parcel B. (a) Horizontal vorticity magnitudes of the different vorticity parts; (b) vertical vorticity parts. Note the different time intervals in each panel.

would result in unbounded growth, but it is offset by diffusion. The relevant vorticity that maintains the vortex is thus infinitely thin and located at the symmetry axis $r = 0$. All parcels outside the symmetry axis acquire their vorticity via diffusion. The vertical vorticity is never exhausted because the vortex line terminates at $z = 0$ where the vertical velocity is zero. In real-world vortices, the vorticity in the inner core must be supplied continuously, in the case of a mature tornado mainly via upward tilting of horizontal vorticity at the base of the vortex (e.g., Fischer and Dahl 2022). Incidentally, drain vortices likewise need a continuous source of vertical vorticity to persist (Yokoyama et al. 2012).

The implication is that parcels that acquire vertical vorticity via diffusion do not maintain the core vorticity and hence do not actively partake in vortex maintenance—these parcels merely benefit from large vorticity in the central core. Analogous arguments apply to the horizontal vorticity: Another process must have created large horizontal vorticity gradients in order for parcels to acquire horizontal vorticity via diffusive processes. Diffusion can thus not be invoked to explain vortex maintenance.

c. *Connection to angular momentum conservation*

At first sight, an easier perspective of vortex maintenance, rather than using vorticity dynamics, may be to consider angular momentum (or perhaps more appropriately, circulation) conservation. Here, the air outside the vortex core has approximately zero vertical vorticity while the swirl velocity of air parcels increases as they converge toward the vortex center. In other words, the airflow just outside the vortex core, where still much of the damage associated with a tornado occurs, has no vertical vorticity. One might wonder, then, why the acquisition of vertical vorticity matters. The reason is that the air in the far field has positive circulation only *because* there is a vortex core—without its presence the circulation would be zero, because circulation is determined by the vorticity vectors piercing the surface around which circulation is calculated. Consequently, the average swirl velocity along the boundary of this surface would be zero if the circulation was zero (and conservation of zero angular momentum would not result in increasing swirl velocities upon convergence). The implication is that the angular momentum explanation of vortex maintenance ultimately relies on the mechanisms that maintain the vortex core.

d. *Limitations*

While the analysis suggests that there are rather diverse pathways by which parcels may acquire large near-ground vertical vorticity as they enter a tornado, a shortcoming of this study is the relatively small number of parcels considered. Aside from the problem of parcels descending beneath the lowest scalar model level, the main culprit is the fact that the parcels are subject to strong velocity gradients, potentially rendering (i) the trajectories themselves and (ii) the vorticity integration, unreliable. Problems such as this one, requiring very small time steps for solutions to converge, are sometimes referred to as stiff (e.g., Shampine et al. 2003) and they are inherently difficult to solve. As a result, while meaningful solutions could be found for only a few parcels, the vast majority of the trajectories could not be used for the analysis. While in the small sample shown in Fig. 4 the vorticity related to surface drag (SGS mixing) dominates, it is not clear how representative this sample is. However, the importance of $\boldsymbol{\omega}_{\mathrm{SGS}}$ in mature TLVs has been highlighted also in previous studies (e.g., Schenkman et al. 2014; Roberts et al. 2016; Roberts and Xue 2017; Fischer and Dahl 2022). Moreover, for our parcels to acquire large horizontal vorticity due to surface drag, they need to be close to the lowest scalar model level (only at the lowest scalar model level the effect of surface drag is included). Unless parcels reached heights of ~10 m AGL, they experience less vorticity production due to surface drag than real-world "near-surface" parcels would experience. Such

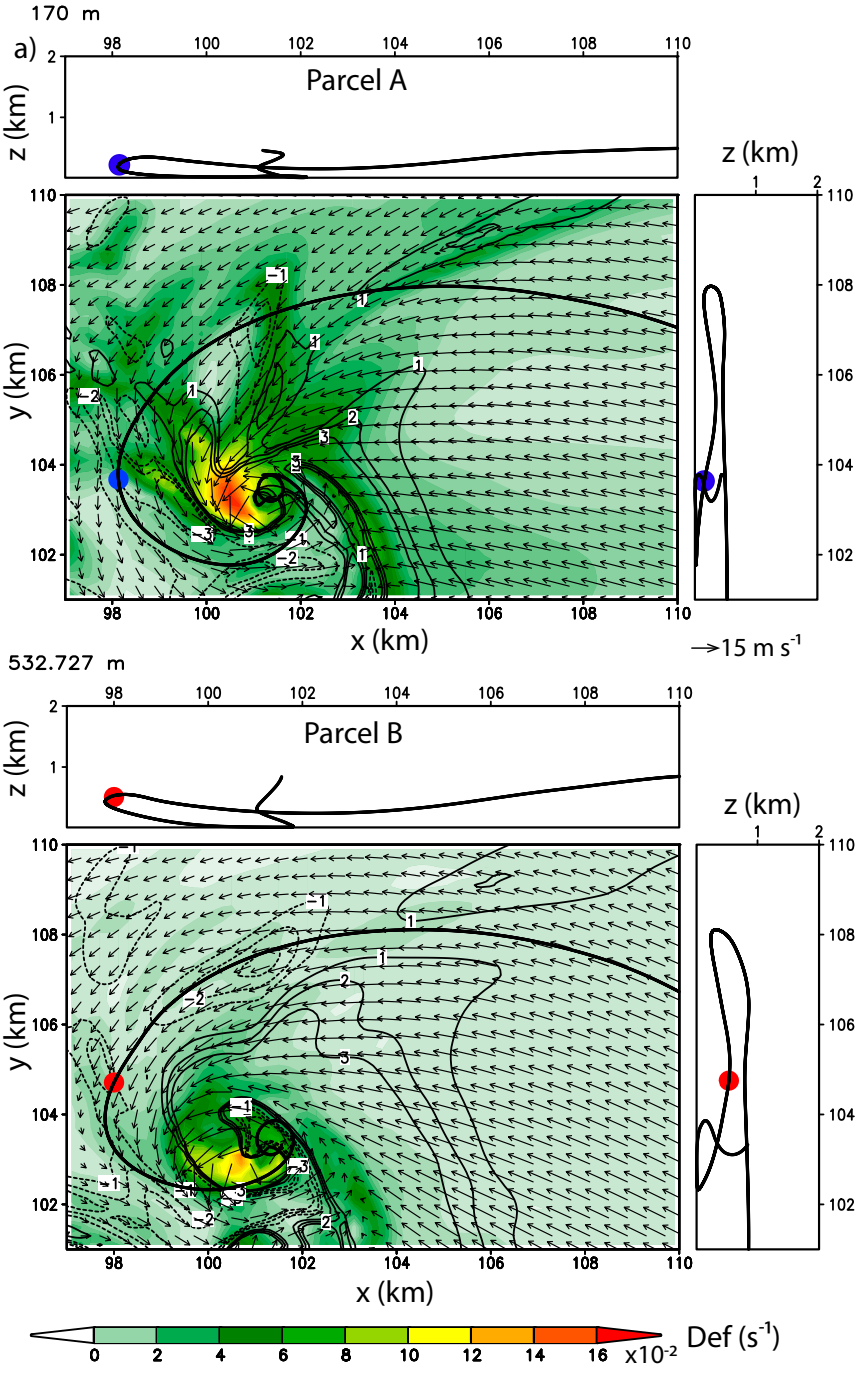

FIG. 14. (a) Magnitude of the 3D the rate-of-strain tensor (shaded) and vertical velocity (contoured in m s^{-1}), as well as storm-relative wind vectors at 170 m AGL, along with the trajectory of parcel A; (b) as in (a), but for parcel B, and the fields are shown at 533 m AGL. The simulation time in both plots is 3840 s.

parcels enter the vortex from within the boundary layer of the tornado, such that they most likely experience significant horizontal vorticity production due to surface drag. This implies that in the present sample the importance of surface drag may still be underestimated.

An alternative to the integration method used here could be to use the material stencils as implemented by Dahl et al. (2014), but the large deformation near the vortex, as well as the requirement that all stencil parcels remain above the lowest scalar model level rendered this technique not as

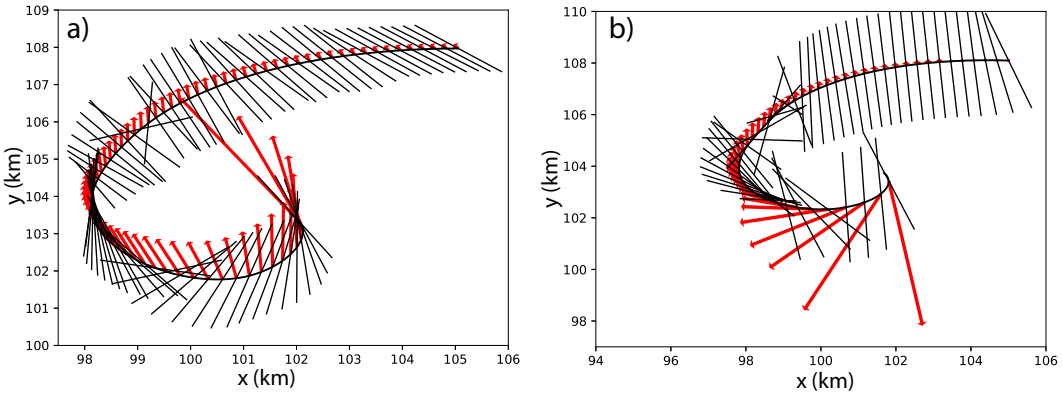

FIG. 15. (a) Horizontal projection of the imported vorticity $\boldsymbol{\omega}_P$ (red arrows) and the intermediate principal axes (black) of the 3D rate-of-strain tensor along the trajectory of parcel A. The time interval shown spans [3400, 4125] s; (b) as in (a), but for parcel B and the time interval [3400, 4145] s.

effective for analyzing an intense vortex. For this reason, Dahl et al. (2014) and Dahl (2015) avoided considering mature vortices, and instead only focused on the weak near-ground "seed" vortex patches, such that the velocity gradients still had relatively small magnitudes and the stencils remained relatively well-behaved. In those settings, a larger number of parcels could be considered, and for these seed vortex patches the robustness of the baroclinic downdraft mechanism could be affirmed (Dahl 2015).

Another possible solution to the small yield of the vorticity source decomposition technique as applied here is to consider the circulation evolution of material circuits. Potential disadvantages are that these circuits tend to become extremely contorted (e.g., Mashiko 2016), possibly rendering the calculations inaccurate, and that only the average partial vorticity component normal to the surface can be identified.

An error source potentially affecting the interpretation of the vorticity source decomposition involves the initial condition. To be able to associate the initial vorticity with the ambient vorticity, long parcel histories are necessary to ensure that the parcels are initially in the unperturbed environment. For that purpose, rather long parcel histories were considered (30 min), but even with such long histories, there were still minor perturbations at the parcels' initial locations (some parcels may have experienced, e.g., small amounts of baroclinic production prior to the beginning of the analysis). The initial vorticity thus did not always perfectly correspond to the base state. Practically, the consequences may be minor, however, given that actual environments are not uniform in the first place, and it is not trivial to even define what constitutes a storm's environment (e.g., Markowski et al. 1998).

These limitations highlight the challenge of obtaining accurate information about vorticity and circulation budgets for concentrated vortices.

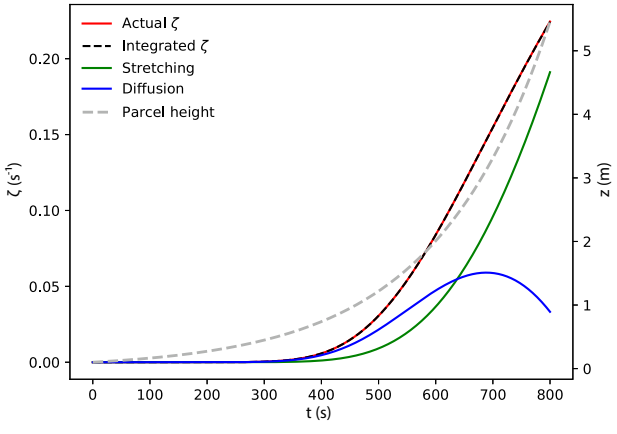

FIG. 16. Time series along a parcel trajectory of the integrated terms of the traditional vertical vorticity equation for the Burgers–Rott vortex, Eq. (52). The parcel height is shown as gray dashed line. Here $r(t = 0) = 500$ m, $z(t = 0) = 0.1$ m, $\nu = 10$ m^2 s^{-1}, $\Gamma = 10^4$ m^2 s^{-1}, and $a = 2.5 \times 10^{-3}$ s^{-1}.

6. Conclusions

Using the CM1 model to simulate an idealized supercell that produced a long-lived tornado-like vortex, we presented the integrals of the traditional vorticity equation along seven trajectories. In addition, the vorticity vector was decomposed into parts that arise from the rearrangement of (i) preexisting (ambient) vorticity, and (ii) vorticity that has subsequently been generated within the storm. The main findings may be summarized as follows:

- The most reliable dynamical source contributing to the rotation of the mature tornado-like vortex is surface drag ($\boldsymbol{\omega}_{\mathrm{SGS}}$), which for all analyzed parcels contributed either positively or, in one case, negligibly, to the vertical vorticity at the base of the vortex (i.e., $\boldsymbol{\omega}_{\mathrm{SGS}}$ never contributed negatively, unlike the other vorticity parts). Baroclinic vorticity contributed positively for the majority, although not all of the parcels. While not the dominant source across the sampled parcels, the preexisting vorticity did directly contribute to the vortex for some parcels. However, given the small sample size ($n = 7$), it

cannot be established how representative these findings are.

- Although the integrated baroclinic vorticity production may seem negligible along a trajectory using the traditional vorticity equation, the subsequent stretching of this initially weak vorticity may lead to large baroclinic vorticity near the vortex as revealed by the vorticity source decomposition. The traditional vorticity analysis in this case emphasizes the importance of tilting and stretching of vorticity, but deemphasizes the importance of small amounts of vorticity production that may end up having a large effect.
- Although numerical diffusion is found to contribute positively to the parcels' vertical vorticity on average, it is shown that diffusion does not aid in maintaining the vortex using the Burgers–Rott model.
- The parcels experience the strongest descent in the occlusion downdraft close to the vortex, rather than in the main downdraft northeast of the mesocyclone. Previous studies have shown that trajectories early in a vortex patch's lifetime are maintained by the downdraft mechanism during which time the contributing parcels descend to the ground in the main downdraft and acquire baroclinically generated vorticity. In contrast, the present analysis suggests that once the vortex matures and the vortex is maintained via abrupt upward tilting of horizontal vorticity at the vortex base, the trajectory topology likewise changes, featuring strong descent mainly in the occlusion downdraft.

Further research is warranted to improve the management of the challenges posed by parcels that descend below the lowest scalar model level, and to increase the accuracy of the integration schemes used to solve the vorticity equations.

Acknowledgments. Discussions about the numerical solvers with Drs. Eric Bruning and Lou Wicker are gratefully acknowledged, as are exchanges with Drs. Paul Markowski and Matt Parker about various aspects about this research. Thanks are extended also to Dr. George Bryan for his ongoing support of the CM1 model and Dr. Brice Coffer for providing the base state for the simulation. Three anonymous reviewers provided valuable comments that improved the presentation. The figures were created using the Python Matplotlib package, as well as the Grid Analysis and Display System (GrADS). Financial support for this study was provided by NSF under Grants AGS-1651786 and AGS-2152537.

Data availability statement. The namelist settings of the CM1 model as well as analysis software are available from the corresponding author upon request.

APPENDIX A

Practical Form of the Vorticity Source Decomposition

In Truesdell's formulation of the vorticity, Eq. (29), the transformation matrices (in this context also referred to as the deformation gradients) need to be known to obtain a solution, but these are not easily available along trajectories obtained from model or radar data. Also, near the vortex the deformation becomes very large, rendering explicit calculation of the deformation gradient (as was done by, e.g., Dahl et al. 2014) inaccurate. As an alternative, Eq. (29) may be differentiated with respect to time, which gives the evolution equation of the individual vorticity parts. The required steps are demonstrated in this appendix. The resulting equations can then be integrated without the need to calculate the transformation matrices.

Before calculating the time derivatives of the vorticity parts inferred from Truesdell's formula, it is noted that the material derivative of $\boldsymbol{\omega}_P$, for example, is given by (e.g., Simmonds 1994, p. 57)

$$\frac{d\boldsymbol{\omega}_P}{dt} = \frac{d}{dt}(\mathbf{g}_k \omega_P^k) = \mathbf{g}_k \frac{d\omega_P^k}{dt} + \omega_P^k \frac{d\mathbf{g}_k}{dt}. \tag{A1}$$

This implies

$$\frac{\delta\omega_P^k}{\delta t} \equiv \frac{d\omega_P^k}{dt} + \mathbf{g}^k \cdot \frac{d\mathbf{g}_i}{dt}\omega_P^i, \tag{A2}$$

where the symbol for the material derivative $\delta/\delta t$ signifies the inclusion of the time derivative of the basis vector $\mathbf{g}_i$ ($\mathbf{g}^k$ is its reciprocal). The extra term on the rhs of Eq. (A2) arises from the time dependence of the basis vector $\mathbf{g}_i$. If this time dependence results from the basis vector field being nonuniform, such that a parcel moving through this field experiences changing basis vectors, the material derivative takes the following form (e.g., Truesdell 1954, p. 42; Simmonds 1994, p. 57):

$$\frac{\delta\omega_P^k}{\delta t} = \frac{d\omega_P^k}{dt} + \Gamma_{ij}^k \omega_P^i \dot{x}^j, \tag{A3}$$

with the dot ($\dot{}$) representing the ordinary time derivative and Γ_{ij}^k being the Christoffel symbol. This correction term is needed for the covariant formulation of the equation: Consider the case where there is uniform flow, but the coordinate basis vectors vary in space. As a result, the coordinate velocity u^k will also vary in space, resulting in spurious accelerations du^k/dt following a parcel. The term involving the Christoffel symbol corrects for these spurious changes and ensures the material derivative honors the tensor transformation law. In Cartesian coordinates the Christoffel symbol is zero.

Now, starting with $\boldsymbol{\omega}_P$ [Eq. (31)],

$$\omega_P^k(t) = \frac{\partial x^k}{\partial \xi^\gamma}(t)\frac{\rho(t)}{\rho(t_0)}\omega_0^\gamma, \tag{A4}$$

and calculating the ordinary time derivative [d/dt part of Eq. (A3)] using the product rule, gives

$$\frac{d\omega_P^k}{dt}(t) = \frac{\partial \dot{x}^k}{\partial \xi^\gamma}(t)\frac{\rho(t)}{\rho(t_0)}\omega_0^\gamma + \frac{\partial x^k}{\partial \xi^\gamma}(t)\frac{\dot{\rho}(t)}{\rho(t_0)}\omega_0^\gamma. \tag{A5}$$

From Eq. (26) with zero torque, it follows that

$$\omega_P^\gamma(t_0) = \frac{\rho(t_0)}{\rho(t)}\omega_P^\gamma(t), \tag{A6}$$

giving

$$\frac{d\omega_P^k(t)}{dt} = \frac{\partial \dot{x}^k}{\partial \xi^\gamma}(t)\frac{\rho(t)}{\rho(t_0)}\frac{\rho(t_0)}{\rho(t)}\omega_P^\gamma(t) + \frac{\partial x^k}{\partial \xi^\gamma}(t)\frac{\dot{\rho}(t)}{\rho(t_0)}\frac{\rho(t_0)}{\rho(t)}\omega_P^\gamma(t). \tag{A7}$$

For notational ease, in the following all variables are assumed to be functions of time t unless otherwise noted. Using the chain rule and noting that $\dot{x}^k = u^k$, one obtains

$$\frac{d\omega_P^k}{dt} = \frac{\partial u^k}{\partial x^i}\frac{\partial x^i}{\partial \xi^\gamma}\omega_P^\gamma + \frac{\partial x^k}{\partial \xi^\gamma}\frac{\dot{\rho}}{\rho}\omega_P^\gamma \tag{A8}$$

$$= \frac{\partial u^k}{\partial x^i}\omega_P^i + \frac{\dot{\rho}}{\rho}\omega_P^k. \tag{A9}$$

While this equation is mathematically correct, the lhs does not describe the physically relevant material rate of change as described in the beginning of this section. The spatial derivatives on the rhs likewise include the effects of the nonuniform basis and thus include spurious effects depending on the choice of the coordinates. Mathematically this is reflected by the fact that Eq. (A9) is not a tensor equation. To fix this problem, we write

$$\frac{\delta\omega_P^k}{\delta t} = \left(\frac{\partial u^k}{\partial x^i} + \Gamma_{ij}^k u^j\right)\omega_P^i + \frac{\dot{\rho}}{\rho}\omega_P^k \tag{A10}$$

$$= u_{;i}^k\omega_P^i + \frac{\dot{\rho}}{\rho}\omega_P^k, \tag{A11}$$

which is the proper tensorial formulation, with the covariant derivative on the rhs [$\partial u^k/\partial x^i$ in Eq. (A9) becomes $u_{;i}^k$]. In symbolic form, we write

$$\frac{d\boldsymbol{\omega}_P}{dt} = \boldsymbol{\omega}_P\cdot\boldsymbol{\nabla}\mathbf{v} - \boldsymbol{\omega}_P(\boldsymbol{\nabla}\cdot\mathbf{v}), \tag{A12}$$

where mass continuity, $\dot{\rho}/\rho = -\boldsymbol{\nabla}\cdot\mathbf{v}$, has been used. Integrating in time gives the imported preexisting vorticity:

$$\boldsymbol{\omega}_P = \boldsymbol{\omega}(t_0) + \int_{t_0}^t dt'[\boldsymbol{\omega}_P(t')\cdot\boldsymbol{\nabla}\mathbf{v}(t') - \boldsymbol{\omega}_P(t')\boldsymbol{\nabla}\cdot\mathbf{v}(t')]. \tag{A13}$$

The initial condition is $\omega_P^k(t_0) = \omega^k(t_0)$, per Eq. (31).

The vorticity parts arising from the torques due to the nonconservative forces (pressure-gradient, mixing, and Coriolis forces) are included in Eq. (32),

$$\omega_N^k = \frac{\partial x^k}{\partial \xi^\gamma}\int_{t_0}^t dt'\frac{\rho(t)}{\rho(t')}\frac{\partial \xi^\gamma}{\partial x^i}(t')\tau_N^i(t'), \tag{A14}$$

where the subscript $N \in \{\text{BC, SGS, DIFF, COR}\}$. Following the same approach as above, we write

$$\frac{d\omega_N^k}{dt} = \frac{d}{dt}\left[\frac{\partial x^k}{\partial \xi^\gamma}\rho\int_{t_0}^t dt'\frac{1}{\rho(t')}\frac{\partial \xi^\gamma}{\partial x^i}(t')\tau_N^i(t')\right]. \tag{A15}$$

Using again the product rule as well as the first fundamental theorem of calculus:

$$\frac{d\omega_N^k}{dt} = \frac{\partial u^k}{\partial x^j}\frac{\partial x^j}{\partial \xi^\gamma}\rho\int_{t_0}^t dt'\frac{1}{\rho(t')}\frac{\partial \xi^\gamma}{\partial x^i}(t')\tau_N^i(t') \tag{A16}$$

$$+ \frac{\partial x^k}{\partial \xi^\gamma}\dot{\rho}\int_{t_0}^t dt'\frac{1}{\rho(t')}\frac{\partial \xi^\gamma}{\partial x^i}(t')\tau_N^i(t') \tag{A17}$$

$$+ \frac{\partial x^k}{\partial \xi^\gamma}\rho\left[\frac{1}{\rho(t)}\frac{\partial \xi^\gamma}{\partial x^i}(t)\tau_N^i(t)\right]. \tag{A18}$$

Now again accounting for the nonuniform basis thus ensuring proper tensor behavior,

$$\frac{\delta\omega_N^k}{\delta t} = u_{;j}^k\frac{\partial x^j}{\partial \xi^\gamma}\rho\int_{t_0}^t dt'\frac{1}{\rho(t')}\frac{\partial \xi^\gamma}{\partial x^i}(t')\tau_N^i(t') \tag{A19}$$

$$+ \frac{\partial x^k}{\partial \xi^\gamma}\dot{\rho}\int_{t_0}^t dt'\frac{1}{\rho(t')}\frac{\partial \xi^\gamma}{\partial x^i}(t')\tau_N^i(t') \tag{A20}$$

$$+ \frac{\partial x^k}{\partial \xi^\gamma}\rho\left(\frac{1}{\rho}\frac{\partial \xi^\gamma}{\partial x^i}\tau_N^i\right). \tag{A21}$$

Based on Eq. (32), we know that

$$\omega_N^\gamma = \int_{t_0}^t dt'\frac{\rho(t)}{\rho(t')}\frac{\partial \xi^\gamma}{\partial x^i}(t')\tau_N^i(t'), \tag{A22}$$

such that

$$\frac{\delta\omega_N^k}{\delta t} = u_{;j}^k\frac{\partial x^j}{\partial \xi^\gamma}\omega_N^\gamma + \frac{\dot{\rho}}{\rho}\frac{\partial x^k}{\partial \xi^\gamma}\omega_N^\gamma + \delta_i^k\tau_N^i \tag{A23}$$

$$= u_{;j}^k\omega_N^j + \frac{\dot{\rho}}{\rho}\omega_N^k + \tau_N^k. \tag{A24}$$

In symbolic form, using mass continuity,

$$\frac{d\boldsymbol{\omega}_N}{dt} = \boldsymbol{\omega}_N\cdot\boldsymbol{\nabla}\mathbf{v} - \boldsymbol{\omega}_N(\boldsymbol{\nabla}\cdot\mathbf{v}) + \boldsymbol{\tau}_N. \tag{A25}$$

Integrating this equation gives

$$\boldsymbol{\omega}_N = \boldsymbol{\omega}_N(t_0) + \int_{t_0}^t dt'[\boldsymbol{\omega}_N(t')\cdot\boldsymbol{\nabla}\mathbf{v}(t') - \boldsymbol{\omega}_N(t')\boldsymbol{\nabla}\cdot\mathbf{v}(t') + \boldsymbol{\tau}_N(t')]. \tag{A26}$$

The initial condition, $\omega_N^k(t_0) = 0$, follows from Eq. (32). Upon inspection of Eqs. (A12) and (A25), it is clear that both equations have the form of Eq. (A25) if $\boldsymbol{\tau}_N$ includes the preexisting part, so that

$$\boldsymbol{\tau}_P = \mathbf{0}, \tag{A27}$$

$$\boldsymbol{\tau}_{\text{BC}} = \boldsymbol{\nabla}\times\left(-\frac{1}{\rho}\boldsymbol{\nabla}p\right), \tag{A28}$$

$$\boldsymbol{\tau}_{\mathrm{SGS}} = \boldsymbol{\nabla} \times \mathbf{f}_{\mathrm{sgs}}, \tag{A29}$$

$$\boldsymbol{\tau}_{\mathrm{DIFF}} = \boldsymbol{\nabla} \times \mathbf{f}_{\mathrm{diff}}, \tag{A30}$$

and

$$\boldsymbol{\tau}_{\mathrm{COR}} = \boldsymbol{\nabla} \times (-f\mathbf{k} \times \mathbf{v}_h'). \tag{A31}$$

The sum $\sum_N \boldsymbol{\omega}_N$ gives the total vorticity. Since this vorticity analysis pertains to the relative vorticity on an f plane, the Coriolis acceleration is treated as "source" term; if one were to consider the absolute vorticity in an inertial reference frame, the planetary vorticity would be included in the $\boldsymbol{\omega}_P$ part (e.g., Dutton 1976, p. 390).

APPENDIX B

Numerical Integration of the Vorticity Equations

We start by introducing the abbreviations

$$\gamma \equiv \frac{\Delta t}{2}, \tag{B1}$$

$$\delta_n \equiv (\nabla \cdot \mathbf{v})_n, \tag{B2}$$

where n is the time step and Δt is the time interval (0.5 s in this case). Then, the trapezoidal scheme for the vorticity equation may be written as

$$\begin{aligned}\boldsymbol{\omega}_{n+1} = \boldsymbol{\omega}_n &+ \gamma(\boldsymbol{\omega}_n \cdot \boldsymbol{\nabla}\mathbf{v}_n - \boldsymbol{\omega}_n\delta_n + \boldsymbol{\tau}_n) \\ &+ \gamma(\boldsymbol{\omega}_{n+1} \cdot \boldsymbol{\nabla}\mathbf{v}_{n+1} - \boldsymbol{\omega}_{n+1}\delta_{n+1} + \boldsymbol{\tau}_{n+1}).\end{aligned} \tag{B3}$$

If the velocity gradients and the forcings ($\boldsymbol{\tau}$) are known for all time steps along the trajectory, which is the case for the traditional integration, the different terms on the rhs of (B3) can be readily obtained. In case of the vorticity source decomposition, $\boldsymbol{\omega}_{n+1}$ on the rhs is unknown, however. In this case, either an iterative approach, such as a Runge–Kutta scheme, can be used to estimate the values at step $n + 1$, or an implicit scheme may be employed, which in this study proved computationally least expensive. To obtain the implicit formulation, all unknown $n + 1$ terms are moved to the lhs of Eq. (B3), giving

$$\begin{aligned}\boldsymbol{\omega}_{n+1} \cdot [-\gamma\boldsymbol{\nabla}\mathbf{v}_{n+1} + \gamma\delta_{n+1}\mathbf{I} + \mathbf{I}] = \boldsymbol{\omega}_n &+ \gamma[\boldsymbol{\omega}_n \cdot \boldsymbol{\nabla}\mathbf{v}_n - \boldsymbol{\omega}_n\delta_n \\ &+ \boldsymbol{\tau}_n + \boldsymbol{\tau}_{n+1}].\end{aligned} \tag{B4}$$

Symbolically, this equation has the form $\mathbf{A} \cdot \mathbf{x} = \mathbf{b}$, which can be solved for $\mathbf{x}$ with the matrix

$$\mathbf{A} = \begin{bmatrix} 1 - \gamma(u_x - \delta) & -\gamma u_y & -\gamma u_z \\ -\gamma v_x & 1 - \gamma(v_y - \delta) & -\gamma v_z \\ -\gamma w_x & -\gamma w_y & 1 - \gamma(w_z - \delta) \end{bmatrix}_{n+1}, \tag{B5}$$

where the subscripts designate partial derivatives; the known vector $\mathbf{b}$, given by

$$\mathbf{b} = \boldsymbol{\omega}_n + \gamma[\boldsymbol{\omega}_n \cdot \boldsymbol{\nabla}\mathbf{v}_n - \boldsymbol{\omega}_n\delta_n + \boldsymbol{\tau}_n + \boldsymbol{\tau}_{n+1}]; \tag{B6}$$

and the desired vorticity vector at step $n + 1$, which is represented by

$$\mathbf{x} = (\xi, \eta, \zeta)^{\mathrm{T}}_{n+1}. \tag{B7}$$

The solution of this system of linear equations may readily be obtained using standard solvers.

REFERENCES

Aris, R., 1962: *Vectors, Tensors, and the Basic Equations of Fluid Mechanics*. Dover Publications, 286 pp.

Boyer, C. H., and J. M. L. Dahl, 2020: The mechanisms responsible for large near-surface surface vertical vorticity within simulated supercellular and quasi-linear storm modes. *Mon. Wea. Rev.*, **148**, 4281–4297, https://doi.org/10.1175/MWR-D-20-0082.1.

Bryan, G. H., and J. M. Fritsch, 2002: A benchmark simulation for moist nonhydrostatic numerical models. *Mon. Wea. Rev.*, **130**, 2917–2928, https://doi.org/10.1175/1520-0493(2002)130<2917:ABSFMN>2.0.CO;2.

Coffer, B. E., and M. D. Parker, 2017: Simulated supercells in nontornadic and tornadic VORTEX2 environments. *Mon. Wea. Rev.*, **145**, 149–180, https://doi.org/10.1175/MWR-D-16-0226.1.

Coriton, B., and J. H. Frank, 2016: Experimental study of vorticity-strain rate interaction in turbulent partially premixed jet flames using tomographic particle image velocimetry. *Phys. Fluids*, **28**, 025109, https://doi.org/10.1063/1.4941528.

Dahl, J. M. L., 2015: Near-ground rotation in simulated supercells: On the robustness of the baroclinic mechanism. *Mon. Wea. Rev.*, **143**, 4929–4942, https://doi.org/10.1175/MWR-D-15-0115.1.

——, 2017: Tilting of horizontal shear vorticity and the development of updraft rotation in supercell thunderstorms. *J. Atmos. Sci.*, **74**, 2997–3020, https://doi.org/10.1175/JAS-D-17-0091.1.

——, 2020: Near-surface vortex formation in supercells from the perspective of vortex patch dynamics. *Mon. Wea. Rev.*, **148**, 3533–3547, https://doi.org/10.1175/MWR-D-20-0080.1.

——, M. D. Parker, and L. J. Wicker, 2014: Imported and storm-generated near-ground vertical vorticity in a simulated supercell. *J. Atmos. Sci.*, **71**, 3027–3051, https://doi.org/10.1175/JAS-D-13-0123.1.

Davies-Jones, R., 1991: The frontogenetical forcing of secondary circulations. Part I: The duality and generalization of the **Q** vector. *J. Atmos. Sci.*, **48**, 497–509, https://doi.org/10.1175/1520-0469(1991)048<0497:TFFOSC>2.0.CO;2.

——, 2000: A Lagrangian model for baroclinic genesis of mesoscale vortices. Part I: Theory. *J. Atmos. Sci.*, **57**, 715–736, https://doi.org/10.1175/1520-0469(2000)057<0715:ALMFBG>2.0.CO;2.

——, 2006: Integrals of the vorticity equation. Part I: General three- and two-dimensional flows. *J. Atmos. Sci.*, **63**, 598–610, https://doi.org/10.1175/JAS3646.1.

——, 2008: Can a descending rain curtain in a supercell instigate tornadogenesis barotropically? *J. Atmos. Sci.*, **65**, 2469–2497, https://doi.org/10.1175/2007JAS2516.1.

——, 2015: Formulas for parcel velocity and vorticity in a rotating coordinate system. *J. Atmos. Sci.*, **72**, 3908–3922, https://doi.org/10.1175/JAS-D-15-0015.1.

——, 2021: Invented forces in supercell models. *J. Atmos. Sci.*, **78**, 2927–2939, https://doi.org/10.1175/JAS-D-21-0082.1.

——, 2022: Theory of parcel vorticity evolution in supercell-like flows. *J. Atmos. Sci.*, **79**, 1253–1270, https://doi.org/10.1175/JAS-D-21-0178.1.

——, and H. E. Brooks, 1993: Mesocyclogenesis from a theoretical perspective. *The Tornado: Its Structure, Dynamics, Prediction, and Hazards*, *Geophys. Monogr.*, Vol. 79, Amer. Geophys. Union, 105–114, https://doi.org/10.1029/GM079p0105.

Dutton, J. A., 1976: *The Ceaseless Wind*. McGraw-Hill, 579 pp.

Epifanio, C. C., and D. R. Durran, 2002: Lee-vortex formation in free-slip stratified flow over ridges. Part II: Mechanisms of vorticity and PV production in nonlinear viscous wakes. *J. Atmos. Sci.*, **59**, 1166–1181, https://doi.org/10.1175/1520-0469(2002)059<1166:LVFIFS>2.0.CO;2.

Fischer, J., and J. M. L. Dahl, 2022: Transition of near-ground vorticity dynamics during tornadogenesis. *J. Atmos. Sci.*, **79**, 467–483, https://doi.org/10.1175/JAS-D-21-0181.1.

Hamlington, P. E., J. Schumacher, and W. J. A. Dahm, 2008: Local and nonlocal strain rate fields and vorticity alignment in turbulent flows. *Phys. Rev.*, **77E**, 026303, https://doi.org/10.1103/PhysRevE.77.026303.

Klemp, J. B., and R. Rotunno, 1983: A study of the tornadic region within a supercell thunderstorm. *J. Atmos. Sci.*, **40**, 359–377, https://doi.org/10.1175/1520-0469(1983)040<0359:ASOTTR>2.0.CO;2.

Kundu, P. K., and I. M. Cohen, 2008: *Fluid Mechanics*. Academic Press, 872 pp.

Markowski, P. M., 2016: An idealized numerical simulation investigation of the effects of surface drag on the development of near-surface vertical vorticity in supercell thunderstorms. *J. Atmos. Sci.*, **73**, 4349–4385, https://doi.org/10.1175/JAS-D-16-0150.1.

——, and Y. Richardson, 2010: *Mesoscale Meteorology in Midlatitudes*. Wiley-Blackwell, 407 pp.

——, and ——, 2014: The influence of environmental low-level shear and cold pools on tornadogenesis: Insights from idealized simulations. *J. Atmos. Sci.*, **71**, 243–275, https://doi.org/10.1175/JAS-D-13-0159.1.

——, and G. H. Bryan, 2016: Les of laminar flow in the PBL: A potential problem for convective storm simulations. *Mon. Wea. Rev.*, **144**, 1841–1850, https://doi.org/10.1175/MWR-D-15-0439.1.

——, J. M. Straka, E. N. Rasmussen, and D. O. Blanchard, 1998: Variability of storm-relative helicity during VORTEX. *Mon. Wea. Rev.*, **126**, 2959–2971, https://doi.org/10.1175/1520-0493(1998)126<2959:VOSRHD>2.0.CO;2.

——, Y. Richardson, and G. Bryan, 2014: The origins of vortex sheets in a simulated supercell thunderstorm. *Mon. Wea. Rev.*, **142**, 3944–3954, https://doi.org/10.1175/MWR-D-14-00162.1.

Marsden, J. E., and T. J. R. Hughes, 1983: *Mathematical Foundations of Elasticity*. Prentice-Hall, 556 pp.

Mashiko, W., 2016: A numerical study of the 6 May 2012 Tsukuba City supercell tornado. Part II: Mechanisms of tornadogenesis. *Mon. Wea. Rev.*, **144**, 3077–3098, https://doi.org/10.1175/MWR-D-15-0122.1.

Parker, M. D., 2014: Composite VORTEX2 supercell environments from near-storm soundings. *Mon. Wea. Rev.*, **142**, 508–529, https://doi.org/10.1175/MWR-D-13-00167.1.

——, and J. M. L. Dahl, 2015: Production of near-surface vertical vorticity by idealized downdrafts. *Mon. Wea. Rev.*, **143**, 2795–2816, https://doi.org/10.1175/MWR-D-14-00310.1.

Rasmussen, E. N., and D. O. Blanchard, 1998: A baseline climatology of sounding-derived supercell and tornado forecast parameters. *Wea. Forecasting*, **13**, 1148–1164, https://doi.org/10.1175/1520-0434(1998)013<1148:ABCOSD>2.0.CO;2.

Roberts, B., and M. Xue, 2017: The role of surface drag in mesocyclone intensification leading to tornadogenesis within an idealized supercell simulation. *J. Atmos. Sci.*, **74**, 3055–3077, https://doi.org/10.1175/JAS-D-16-0364.1.

——, ——, A. D. Schenkman, and D. T. Dawson, 2016: The role of surface drag in tornadogenesis within an idealized supercell simulation. *J. Atmos. Sci.*, **73**, 3371–3395, https://doi.org/10.1175/JAS-D-15-0332.1.

Salmon, R., 1998: *Geophysical Fluid Dynamics*. Oxford University Press, 378 pp.

Schenkman, A. D., M. Xue, and M. Hu, 2014: Tornadogenesis in a high-resolution simulation of the 8 May 2003 Oklahoma City supercell. *J. Atmos. Sci.*, **71**, 130–154, https://doi.org/10.1175/JAS-D-13-073.1.

——, ——, and D. T. Dawson, 2016: The cause of internal outflow surges in a high-resolution simulation of the 8 May 2003 Oklahoma City tornadic supercell. *J. Atmos. Sci.*, **73**, 353–370, https://doi.org/10.1175/JAS-D-15-0112.1.

Shampine, L. F., I. Gladwell, and S. Thompson, 2003: *Solving ODEs with MATLAB*. Cambridge University Press, 263 pp.

Simmonds, J. G., 1994: *A Brief on Tensor Analysis*. Springer, 112 pp.

Truesdell, C., 1954: *The Kinematics of Vorticity*. Indiana University Press, 232 pp.

Vande Guchte, A., and J. M. L. Dahl, 2018: Sensitivities of parcel trajectories beneath the lowest scalar model level of a Lorenz vertical grid. *Mon. Wea. Rev.*, **146**, 1427–1435, https://doi.org/10.1175/MWR-D-17-0190.1.

Walko, R. L., 1993: Tornado spin-up beneath a convective cell: Required basic structure of the near-field boundary layer winds. *The Tornado: Its Structure, Dynamics, Prediction, and Hazards*, *Meteor. Monogr.*, Vol. 79, Amer. Geophys. Union, 89–95, https://doi.org/10.1029/GM079p0089.

Wicker, L. J., and R. B. Wilhelmson, 1995: Simulation and analysis of tornado development and decay within a three-dimensional supercell thunderstorm. *J. Atmos. Sci.*, **52**, 2675–2703, https://doi.org/10.1175/1520-0469(1995)052<2675:SAAOTD>2.0.CO;2.

——, and W. C. Skamarock, 2002: Time-splitting methods for elastic models using forward time schemes. *Mon. Wea. Rev.*, **130**, 2088–2097, https://doi.org/10.1175/1520-0493(2002)130<2088:TSMFEM>2.0.CO;2.

Yokoyama, A., Y. Maruyama, and J. Mizushima, 2012: Origin of the bathtub vortex and its formation mechanism. *J. Phys. Soc. Japan*, **81**, 074401, https://doi.org/10.1143/JPSJ.81.074401.

Zee, A., 2013: *Einstein Gravity in a Nutshell*. Princeton University Press, 888 pp.

CORRIGENDUM

JOHANNES M. L. DAHL[a] AND JANNICK FISCHER[b]

[a] *Department of Geosciences, Texas Tech University, Lubbock, Texas*
[b] *Karlsruher Institut für Technologie, Germany*

(Manuscript received 15 November 2024, in final form 5 December 2024, accepted 5 December 2024)

This corrigendum concerns two equations in Dahl and Fischer's (2023) derivation: one erroneously omitted term in their Eq. (13), which, however, will be shown not to affect the downstream mathematical development, and one typo in Eq. (30).

1. Equation (13)

In the following, the correct form of the time integral of the momentum equation, Eq. (13) in Dahl and Fischer (2023), is presented, and it is demonstrated that an additional term that appears in that equation is irrotational and hence does not contribute to the vorticity integral, Dahl and Fischer's Eq. (14). The momentum equation is given by

$$\frac{d\mathbf{v}}{dt} = \mathbf{f}, \tag{1}$$

where $\mathbf{v}$ is the velocity vector and $\mathbf{f}$ is the net force acting on the fluid parcel. Using the same notation as in Dahl and Fischer (2023), this may be written as

$$\frac{d\mathbf{v}}{dt} = \frac{d}{dt}(u_\alpha \mathbf{g}^\alpha) = \frac{du_\alpha}{dt}\mathbf{g}^\alpha + u_\alpha \frac{d\mathbf{g}^\alpha}{dt} = \mathbf{f}. \tag{2}$$

The term on the rhs involving du_α/dt describes the time rate of change of the coordinate velocity u_α, which includes the effect of the force as well as the effect of the time-dependent coordinate basis vectors. The second term, involving $d\mathbf{g}^\alpha/dt$, is the geometric term that corrects for the effect of the time-dependent coordinate basis. In the present case, the basis vectors change because the material volume, including the coordinate system materially attached to it, is deformed by the flow.[1] To obtain an expression for the time evolution of $\mathbf{g}^\alpha$, we first recognize that

$$\mathbf{g}^\alpha = \nabla \xi^\alpha. \tag{4}$$

Now, for any parcel property Φ, we may write $\Phi(t) = \Phi[\mathbf{r}(t), t]$, where $\mathbf{r}$ is the parcel's location. Using the chain and product rules, we find

[1] In many applications, the coordinate basis is constant in time but nonuniform in space, such that the geometric term is given by (e.g., Simmonds 1994, p. 57)

$$u_\alpha \frac{d\mathbf{g}^\alpha}{dt} = u_\alpha u^\beta \frac{\partial d\mathbf{g}^\alpha}{\partial d\xi^\beta} = -u_\alpha u^\beta \Gamma^\alpha_{\beta\gamma} \mathbf{g}^\gamma \tag{3}$$

where $u^\beta\, \partial \mathbf{g}^\alpha/\partial \xi^\beta$ is the time rate of change of $\mathbf{g}^\alpha$ due to "advection" [see also appendix A of Dahl and Fischer (2023)] and $\Gamma^\alpha_{\beta\gamma}$ is the Christoffel symbol.

Corresponding author: Johannes Dahl, johannes.dahl@ttu.edu

DOI: 10.1175/JAS-D-24-0257.1

$$\nabla\left(\frac{d\Phi}{dt}\right) = \nabla\left(\frac{\partial\Phi}{\partial t} + \mathbf{v}\cdot\nabla\Phi\right) = \frac{d}{dt}(\nabla\Phi) + (\nabla\mathbf{v})\cdot\nabla\Phi. \tag{5}$$

With $\Phi = \xi^\alpha$ and $d\xi^\alpha/dt = 0$, we see that

$$\frac{d\mathbf{g}^\alpha}{dt} = \frac{d}{dt}(\nabla\xi^\alpha) = -(\nabla\mathbf{v})\cdot\nabla\xi^\alpha. \tag{6}$$

The rhs is equivalent to the 3D vector frontogenesis function [vector frontogenesis in 2D is discussed by Keyser et al. (1988)], which connects the evolution of the coordinate curves to the flow field: Like isentropes in the usual frontogenesis case, material coordinate curves are deformed and rotated by the flow; the contravariant basis vectors correspond to the gradients of the isentropes. This implies that the geometric term $\mathbf{G}$ may be written as

$$\mathbf{G} = u_\alpha\frac{d\mathbf{g}^\alpha}{dt} \tag{7}$$

$$= -u_\alpha(\nabla\mathbf{v})\cdot\nabla\xi^\alpha \tag{8}$$

$$= -(\nabla\mathbf{v})\cdot\mathbf{g}^\alpha u_\alpha \tag{9}$$

$$= -(\nabla\mathbf{v})\cdot\mathbf{v}. \tag{10}$$

With this, the momentum equation becomes

$$\frac{\delta u_\beta}{\delta t} = \frac{du_\beta}{dt} - \mathbf{g}_\beta\cdot[(\nabla\mathbf{v})\cdot\mathbf{v}] = f_\beta. \tag{11}$$

This equation is equivalent to Eq. (12) in Dahl and Fischer (2023). When integrating this equation with respect to time, however, the geometric term needs to be carried along, so Dahl and Fischer's Eq. (13) should read

$$u_\beta(t) = u_\beta(t_0) + \int_{t_0}^{t} dt' f_\beta(t') + \int_{t_0}^{t} dt'\mathbf{g}_\beta(t')\cdot\{[\nabla\mathbf{v}(t')]\cdot\mathbf{v}(t')\}. \tag{12}$$

When this equation is inserted into the expression for the vorticity,

$$\omega^\gamma(t) = \frac{\epsilon^{\alpha\beta\gamma}}{\sqrt{G(t)}}\frac{\partial u_\beta(t)}{\partial\xi^\alpha}, \tag{13}$$

one obtains

$$\omega^\gamma(t) = \frac{\epsilon^{\alpha\beta\gamma}}{\sqrt{G(t)}}\frac{\partial u_\beta(t_0)}{\partial\xi^\alpha} + \int_{t_0}^{t} dt'\frac{\epsilon^{\alpha\beta\gamma}}{\sqrt{G(t)}}\frac{\partial f_\beta(t')}{\partial\xi^\alpha} + \int_{t_0}^{t} dt'\frac{\epsilon^{\alpha\beta\gamma}}{\sqrt{G(t)}}\frac{\partial}{\partial\xi^\alpha}\{\mathbf{g}_\beta(t')\cdot[\nabla\mathbf{v}(t')\cdot\mathbf{v}(t')]\}. \tag{14}$$

This equation corresponds to Eq. (14) in Dahl and Fischer (2023), but it includes the geometric term (the last term on the rhs). To show that this term is zero, we use Eq. (23) from Dahl and Fischer (2023) and find that

$$\int_{t_0}^{t} dt'\frac{\epsilon^{\alpha\beta\gamma}}{\sqrt{G(t)}}\frac{\partial}{\partial\xi^\alpha}\{\mathbf{g}_\beta(t')\cdot[\nabla\mathbf{v}(t')\cdot\mathbf{v}(t')]\} = -\int_{t_0}^{t} dt'\frac{\rho(t)}{\rho(t')}\frac{\epsilon^{\alpha\beta\gamma}}{\sqrt{G(t')}}\frac{\partial G_\beta(t')}{\partial\xi^\alpha} \tag{15}$$

$$= -\int_{t_0}^{t} dt'\frac{\rho(t)}{\rho(t')}[\nabla\times\mathbf{G}(t')]^\gamma \tag{16}$$

$$= -\int_{t_0}^{t} dt'\frac{\rho(t)}{\rho(t')}\mathbf{g}^\gamma(t')\cdot[\nabla\times\mathbf{G}(t')]. \tag{17}$$

If $\nabla\times\mathbf{G} = \mathbf{0}$, this integral vanishes. To see that this is indeed the case, we first apply the product rule and see that

$$\mathbf{G} = -(\nabla \mathbf{v}) \cdot \mathbf{v} = -\frac{1}{2}\nabla(\mathbf{v} \cdot \mathbf{v}) = -\frac{1}{2}\nabla V^2, \tag{18}$$

where $V = \sqrt{\mathbf{v} \cdot \mathbf{v}}$ is the velocity magnitude. Then,[2]

$$\nabla \times \mathbf{G} = -\frac{1}{2}\nabla \times \nabla V^2 \equiv \mathbf{0}. \tag{19}$$

2. Equation (30)

Equation (30) in Dahl and Fischer (2023) is written in symbolic form, so there should be no index on the lhs. The correct equation is given by

$$\boldsymbol{\omega}(t) = \frac{\partial \mathbf{r}}{\partial \boldsymbol{\xi}}(t) \cdot \left[\frac{\rho(t)}{\rho(t_0)} \boldsymbol{\omega}_0 + \int_{t_0}^{t} dt' \, \frac{\rho(t)}{\rho(t')} \frac{\partial \boldsymbol{\xi}}{\partial \mathbf{r}}(t') \cdot \boldsymbol{\tau}(t') \right]. \tag{20}$$

Acknowledgments. Exchanges with Drs. Bob Davies-Jones and Giorgio Bornia led to a more general and simplified treatment.

REFERENCES

Dahl, J. M. L., and J. Fischer, 2023: On the origins of vorticity in a simulated tornado-like vortex. *J. Atmos. Sci.*, **80**, 1361–1380, https://doi.org/10.1175/JAS-D-22-0145.1.

Keyser, D., M. J. Reeder, and R. J. Reed, 1988: A generalization of Petterssen's frontogenesis function and its relation to the forcing of vertical motion. *Mon. Wea. Rev.*, **116**, 762–781, https://doi.org/10.1175/1520-0493(1988)116<0762:AGOPFF>2.0.CO;2.

Simmonds, J. G., 1994: *A Brief on Tensor Analysis*. Springer, 112 pp.

[2] Note that $(\nabla \mathbf{v}) \cdot \mathbf{v} \triangleq (\partial u_j/\partial x_i) u_j$ is not equal to the advection term $(\mathbf{v} \cdot \nabla)\mathbf{v} \triangleq u_i(\partial u_j/\partial x_i)$, whose curl is generally not zero.